UNIVERSITY OF NAPLES "FEDERICO II"

DEPARTMENT OF INDUSTRIAL ENGINEERING

DIVISION OF MECHANICAL AND ENERGY ENGINEERING

Ph. D. Thesis

XXVI Cycle

EULERIAN – LAGRANGIAN DESCRIPTION OF STIRRING AND MIXING IN TRANSITIONAL FLOW. INTERCONNECTIONS WITH AUTOIGNITING STRUCTURES.

Supervisor
Prof. Antonio CAVALIERE

Author
Eng. Diego SCARPA

March 2014

"Remember that all models are wrong; the practical question is how wrong do they have to be to not be useful."

George E. P. Box

UNIVERSITY OF NAPLES "FEDERICO II"

DEPARTMENT OF INDUSTRIAL ENGINEERING

DIVISION OF MECHANICAL AND ENERGY ENGINEERING

Abstract

Doctor of Philosophy

EULERIAN – LAGRANGIAN DESCRIPTION OF STIRRING AND MIXING IN TRANSITIONAL FLOW. INTERCONNECTIONS WITH AUTOIGNITING STRUCTURES.

by Diego SCARPA

Turbulent non-premixed combustion has a particular relevance since in common devices involved flows are inevitably turbulent and separated before their injection in combustion chambers.

In particular, non-premixed combustion can be viewed as a three stage process of stirring, diffusion and ignition spanning the full spectrum of space-time scales of the flow.

In particular, an exact description of stirring phenomena is given by the location of the interface between the flows.

The related scales of the passive scalar transport has also been the main topic of numerous publications, but there are still open questions related to mixing-relevant flows.

The main purpose of this thesis is to show that enucleating the stirring process from the mixing process is one of the most convenient way to face with this problem and that the quantitative assessment of some related stirring characteristics is feasible on one side as well as sufficient to describe the mixing pattern on the other side. The selection of some "critical" quantities to be

evaluated on the interface for their exploitation in a mixing characterization should include also significant Lagrangian quantities.

Moreover, the ignition processes involved on the interface results strictly interconnected with the advected-surfaces evolution.

Therefore the evaluation of the stirring/mixing quantities lays the foundation for a sequentially-structured approach to characterize non-premixed combustion flows.

In this context, a description of the autoigniting structures in term of gaseous diffusion flames seems to be useful.

Keywords: Stirring, Mixing, Lagrangian surfaces, Autoignition.

Contents

List of Figures

Abbreviations

CFD	**C**omputational **F**luid **D**ynamics
DNS	**D**irect **N**umerical **S**imulation
DPM	**D**iscrete **P**hase **M**odel
HFDO	**H**ot **F**uel **D**iluted **O**xidant
HODO	**H**ot **O**xidant **D**iluted **O**xidant
IDW	**I**nverse **D**istance **W**eighting
LES	**L**arge **E**ddy **S**imulation
LCS	**L**agrangian **C**oherent **S**tructures
MILD	**M**oderate or **I**ntense **L**evel of **D**ilution
ODE	**O**rdinary **D**ifferential **E**quations
PDE	**P**artial **D**ifferential **E**quations
PDF	**P**robability **D**ensity **F**unction
PIV	**P**article **I**mage **V**elocimetry

PRT **P**articles **R**esidence **T**ime

Dimensionless Numbers

Damkohler numbers

$$\begin{cases} Da = \dfrac{reaction\ rate}{convective\ mass\ transport\ rate} = kC_0^{n-1}\tau \\ Da_{II} = \dfrac{reaction\ rate}{diffusive\ mass\ transport\ rate} = \dfrac{kC_0^{n-1}}{k_g A} \end{cases}$$

Stokes number

$$Stk = \frac{characteristic\ time\ of\ a\ particle}{characteristic\ time\ of\ the\ flow} = \frac{\tau_r V}{d_c}$$

Schmidt number

$$Sc = \frac{viscous\ diffusion\ rate}{molecular\ (mass)\ diffusion\ rate} = \frac{\nu}{\mathcal{D}} = \frac{\mu}{\rho\mathcal{D}}$$

Reynolds number

$$Re = \frac{inertial\ forces}{viscous\ forces} = \frac{\rho \mathrm{V} d_c}{\mu} = \frac{\mathrm{V} d_c}{\nu}$$

Symbols

A	interfacial area
C	curvature
C_0	initial concentration
$\mathcal{D}$	mass diffusivity
d_c	characteristic dimension
e	coefficient of restitution
$\boldsymbol{I}$	unit tensor
K	stretch rate
K_0	strain rate
k	kinetics reaction rate constant
k_g	global mass transport coefficient
$\dot{m}_p$	mass flow rate of the particle stream
$\mathbf{n}$	normal unit vector
n	reaction order
p	static pressure
r	distance from supporting point
SR	stretch ratio
T	temperature
t	time
u_p	particle velocity
$\boldsymbol{V}$	fluid velocity of the flow
W	mass fraction of generic species

w	interpolation weight
X	molar fraction
x_p	particle coordinates
Z	mixture fraction
Z_{MR}	most reactive mixture fraction

Greek symbols

β	a conserved variable per unit mass
γ	stretching factor
ΔT_{max}	maximum allowable temperature increase
δ_m	diffusive isothermal layer thickness
δ_m^{ns}	unstretched diffusive layer thickness
ε	turbulent kinetic energy dissipation rate
η	Kolmogorov length scale
θ	impact angle
λ	wavelength
ν	kinematic viscosity
ξ	Boltzmann variable
μ	dynamic viscosity
ρ	density
$\boldsymbol{\tau}$	stress tensor
τ	mean residence time
τ_{IGN}	minimum ignition time
τ_{MAX}	temperature-maximization time

τ_{STAB}	stabilization time
τ_r	relaxation time of a particle

To my loved ones

Chapter 1

Introduction

Turbulent combustion has been long considered a paradigm for multi-scale problems and has long been identified as one of the important problems to solve, hence the increasing interest from the computational and applied mathematics communities.

In particular, non-premixed combustion can be viewed as a three stage process of stirring, diffusion and ignition spanning the full spectrum of space-time scales of the flow.

In particular, an exact description of stirring phenomena is given by the location of the interface between the flows. Gaseous diffusion flames and their characteristic scales have been object of numberless studies which give a reference framework for an exhaustive evaluation of many well defined problems. The related scales of the passive scalar transport has also been the main topic of numerous publications, but there are still open questions related to mixing-relevant flows. This is quite evident for transitional flows for which "full" Eulerian characterizations of fluid dynamic patterns are available, but for which a fully Lagrangian characterization in partially traced flows is still missing. In particular the category of flows which are on the border of the technological feasibility of the "full" characterization are the dominion of forefront open questions. "Full" characterization is used in this thesis to refer to characterizations which are in the class of Direct Numerical Simulation (DNS) or High resolution Imaging in the case of experiment field. In both case the maximum level of resolution allow to reach a minimum scale for an Eulerian characterization which generates also classes of mixing flows which need higher level of resolution. This is the case for incipient chaotic flows in which the distances of mixing layers, undergoing multiple folding, can be much smaller of

the minimum grid/pixel size used in the "full" characterization of extended not-uniformly distributed parts of the flow. Many experimental and numerical studies show such behavior when residence times are long. For instance in the 2-D visualization this has been observed in the fusion of the material surfaces inside a single pixel.

The coupling among small characteristic length scales, their not uniform distribution and their not steady distribution suggest the need both of using adaptive grids for the simulation of such mixing field and, above all, of finding a way to localize them. The main purpose of this thesis is to show that enucleating the stirring process from the mixing process is one of the most convenient way to face with this problem and that the quantitative assessment of some related stirring characteristics is feasible on one side as well as sufficient to describe the mixing pattern on the other side. More specifically, stirring characterization means characterization of interfaces, which in turn is the discontinuity locus between traced and not-traced flows. This means that it is a surface for a 3-D flow and it is a line for a 2-D flow. In this respect the interface is a way to infer a dimensionality reduction more than a simple feature extraction. Therefore, a very detailed description of the interface, also with higher resolution than that used in the Eulerian characterization of the flow, can be achieved with the same computational/data collection limitation. The construction of the interface for a given Eulerian assigned pattern has to be considered a sort of manifold learning process rather than a simple sequential decoupled numerical evaluation since it can be obtained starting from a sufficiently dense velocity data base obtained with whatever procedure (experimental or numerical) rather than a result data set obtained from a numerical model. Finally it is worth of anticipation as introductive remark that the selection of some critical quantities to be evaluated on the interface for their exploitation in a mixing characterization should include also significant Lagrangian quantities since the mixing layer increase along the time according

to well established laws. As matter of fact the conditional determination of these Lagrangian quantities on the Eulerian interface make this "measurement" an Eulerian-Lagrangian quantity. For example a residence time of a point on an interface is the residence time of the trajectory which intersect the interface in a fixed point, at fixed time.

In Chapter 5 all of these characteristics are presented in sequence, with their definition and the difficulties related to their conditional statistical determination. Their relevance in the mixing characterization is discussed in sections downstream of their effective single-event and statistical determinations obtained on a 2-D transitional flow, which has been selected as test case to analyze complex statistical evaluations. This has been preliminary characterized by means of Eulerian experimental and numerical quantities, presented in Chapter 3 and 4 respectively, which yield equivalent statistical measurements. Then a dense spatial temporal data base, experimentally verified, of velocity components of one flow selected on the ground of the length scale broadness is exploited for the generation and characterization of the interface. Finally the most significant statistical functions are presented and commented in the perspective to be representative of the mixing process and, also when restrictive simplifications are assumed, to be the ground for the formulation of mixing models in low-pass filtering model as Large Eddy Simulation (LES). Definitions of the less conventional quantities (like interface and intermaterial surface) are given in the next Chapter 2 together with more common definitions (conserved variable, mixture fraction).

Moreover, the ignition processes involved on the interface results strictly interconnected with the advected-surfaces evolution.

Therefore the evaluation of the stirring/mixing quantities lays the foundation for a sequentially-structured approach to characterize non-premixed combustion flows.

In this context, a description of the reactive structures in term of gaseous diffusion flames seems to be useful.

In particular, the analysis of the elementary reactive diffusion layers that can be obtained in the lamellar structures related to the interface will be done considering autoigniting systems. Specifically, in MILD Combustion conditions some behaviors different from those obtained in standard combustion conditions has been observed. In these low Da processes, in fact, the reactive zone seems to be represented by a "layerlet" structure.

These aspects will be clarified in Chapter 5 in relation to a specific autoigniting structure characterized by means of unsteady counter-flow diffusion flames.

The main purpose of the project is to make a DNS of air flowing in a 2-D channel with particles injected at the first contact point between two jets and develop a Lagrangian method for investigating data generated by DNS and the particle tracks in MATLAB. The particle tracks should reveal transitional structures that can be analyzed. The goal is develop the tools needed to obtain the fully kinematic characterization and the statistical modelling of interfacial surfaces.

As the main focus is to develop the method to investigate the data generated the choice of different models will not be dealt with at any deeper level. As such simulations will be performed using "best practice" guides and conventional and well tested simulation methods. The validity of DNS will also not be investigated in depth but generally taken to be able to represent reality correctly for the purposes at hand. This is not to say that motivations for the choice of DNS will be completely left out or that an analysis of the validity and appropriateness of DNS will not be conducted at all for instance, but it is not the main focus. Furthermore, the topic of simulation methods in terms of different code packages will not be dealt with at all.

Chapter 2

Definitions

2.1. Conserved and material variables

A variable is conserved if it obeys a source-free balance equation; i.e. it is relative to a quantity which cannot be created or destroyed, but only convected and diffused. This statement is expressed in differential form according to the following equation, reported with classical notation as it can be found in many basic text books [1,2]

$$\rho \frac{\partial \beta}{\partial t} + \rho \boldsymbol{V} \cdot \boldsymbol{\nabla} \beta - \boldsymbol{\nabla} \cdot \left(\rho \mathcal{D}_\beta \boldsymbol{\nabla} \beta \right) = 0 \qquad (2\text{-}1)$$

in which β represents a conserved variable per unit mass.

According to basic physical principles, the total energy and the total mass are conserved. In contrast, the energy associated with a single species or the mass fraction of species are not generally conserved, because they can be converted in other forms of energy and in other kinds of molecular species, respectively. Other examples of conserved variables are the mass of an atomic species, if atomic reaction can be neglected, or the quantities, which are not conserved in principle, but which do not undergo significant conversions in specific cases (for instance inert species in complex reactive systems).

Conserved variables peculiar to the combustion field are obtained as a linear combination of some non-conserved variables. They are described as "coupling functions" or Schvab-Zel'dovich variables [1,2] and are generally used as a combination of mass fractions of the whole fuel and oxidizer, which can be thought as reacting in a single step and in a fixed stoichiometric ratio.

Generalization of this kind of coupled-conserved variable also can be obtained for multi-component media and for combination of molecular species and formation enthalpy. In the latter case a free-source conservation equation of the total enthalpy (including of sensible and formation enthalpies) is considered.

A normalized form of a conserved variable can be defined, in terms of a mixture fraction, as

$$Z = \frac{\beta_l - \beta_{ox}}{\beta_f - \beta_{ox}} \tag{2-2}$$

where subscripts l, f, ox stand for local, fuel and oxidizer, respectively. Therefore, corresponding conserved variables (β_l, β_f, β_{ox}) are defined at all points of mixing flows (subscript l), in the unmixed fuel flow (subscript f) and in the unmixed oxidizer flow (subscript ox), respectively. It is of interest to note that:

- the definition is also used when the two streams are diluted with inert species;
- the values of the mixture fractions, referred to different conserved variables, are equal when they diffuse with the same rate.

Mixture fraction (Z) complies with the same conservation equation of any conserved variable (β), since they differ for fixed quantities, ($\beta_{ox}/(\beta_f - \beta_{ox})$), disappearing in the differentiation and for a factor, $1/(\beta_f - \beta_{ox})$, which can be neglected because it is present in all the terms of the conservation equation. In other words, Equation (2-1) applies also to the mixture fraction when the symbol β is changed with symbol Z.

The sum of the first two terms in Equation (2-1), divided by the density, is designated in the literature as material or substantial derivative. It is cited in the following as D/Dt and it defines a "material" variable, β_M when Equation (2-1) can be written as

$$\frac{D\beta_M}{Dt} = \frac{\partial \beta_M}{\partial t} + \boldsymbol{V} \cdot \boldsymbol{\nabla} \beta_M = 0 \qquad (2\text{-}3)$$

An example of material variable is the mass fraction of a tracer, which we discuss in the next section.

2.2. Tracers

A tracer is defined as an inert substance, uniformly dispersed in part of the flow, in such a weak concentration that the thermal and fluid-dynamic evolution of the flow is not altered [3].

In agreement with [4] the tracer should not only be non-diffusing, but should also be transported at mean field velocity. In this way the tracer's mass fraction, W_t, will be constant in time, and therefore the material derivative of W_t will be zero.

It is quite difficult to produce this kind of tracer under experimental conditions, in order to seed a gaseous flow, also because the tracer cannot be a gas, as gases, by definition, diffuse. Neither can the tracer be a solid particle of such large dimensions to be unable to immediately respond to accelerations in the average flow. In effect the only tracer, having features which are close to those described in the definition above, is a particle for which $Stk < 1$ [5] and for which $Sc > 1000$ [6]. A particle, for instance, between 0.1 and 1 μm is sufficiently large in dimension to ensure that Brownian diffusion is low, but it is sufficiently small to immediately follow a flow. At times the term "tracer"

refers to a diffusive substance (generally featuring a molecular diffusion coefficient equal to the mean coefficient of the substances into which it must diffuse). In such cases it is always better to specify "diffusive tracer" in order to avoid any ambiguity between this and the initial definition. Finally, it is necessary to specify that, in theory, the injection of a tracer into a known flow field is a very simple concept because every particle of the tracer follows the trajectory of a massless point. In practice the integration of the material derivative (DW_t/Dt) in time can present problems associated with the possible chaotic evolution of the trajectories [7]. This is true too when the flow field is well defined as in laminar fields. This behavior is designated Lagrangian turbulence [8].

2.3. Reference surfaces

2.3.1. Eulerian surfaces (interface, isosurface)

When a non-diffusive tracer is introduced into part of the flow it determines an interface. This is the surface of the flow where the concentration of the tracer is discontinuous, that is where it passes from zero to a finite value on an infinitely thin surface. In other words, an interface is the place of the points in space where ∇W_t is infinite.

Examples of interfaces are shown in Figure 2.1 [9]. They are obtained by seeding the central part of a 2-D plane jet with TiO_2 sub-micronic particles. The concentration of the particles is measured by means of elastic light scattering. White corresponds to an area in which the tracer concentration is zero. Black corresponds to an area in which the tracer concentration is equal to that fixed at injection. It is interesting to note that the tracer substance concentration in a material volume cannot, by definition, vary in time.

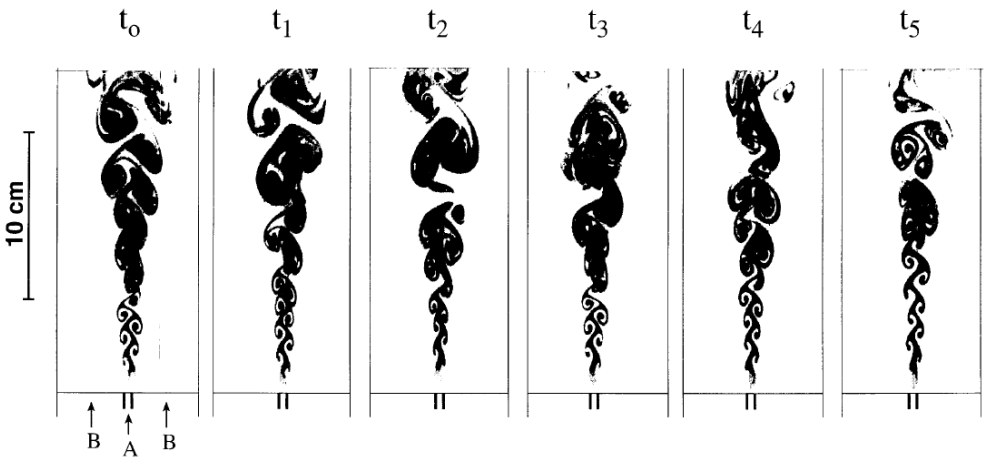

Figure 2.1. Interfaces sequence of a transitional isothermal jet (after Cavaliere 1995).

If the resolution, through which the spatial dispersion of the tracer is observed, is limited, the concentration itself seems to change point by point and even the interface appears as a continuous variation of the tracer concentration. It is also possible that, in practice, the tracer concentration is so weak that its presence is hardly detectable. This happens when the tracer is transported in filamented structures so thin that its continuous distribution does not occur. Despite these experimental difficulties, the interface is a characteristic of the dispersion of one gas into another which is easily measurable, because it possesses a clearly Eulerian nature. In fact, it is possible at any time to obtain a measurement without worrying about the intricate Lagrangian evolution of the particles.

Usually the term *stirring* is applied to the process that leads to extension and dispersion of the interface, in as much as diffusion processes are not used because stirring is purely convective.

Isosurfaces, or iso-level surfaces [10,11], are surfaces on which scalars are constant. For the sake of brevity in this thesis, isosurfaces will be referred to the scalar mixture fraction, Z.

2.3.2. Lagrangian surfaces (material, intermaterial)

Surface is considered material when it is made up of points identified by a tracer. In other words a surface is material when it follows a material evolution [11]. Consider, for example, a 2-D surface at time t_0 as it is sketched through its linear section in Figure 2.2a.

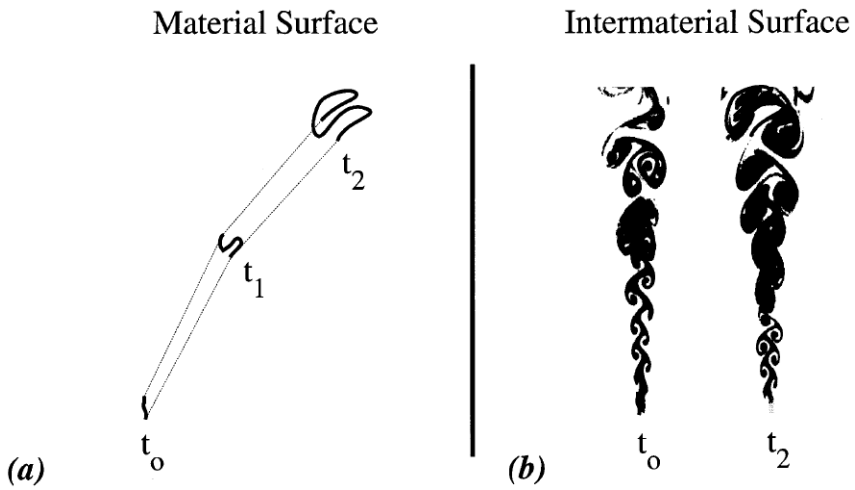

Figure 2.2. (a) Example of material surface evolution. (b) Schematic of intermaterial surface evolution. Two material surfaces are selected on the interfaces at time t_0 and t_2 (after Cavaliere 2001).

Every point of the surface follows a definite trajectory. At time t all these points together will make up a new surface which besides being translated and rotated is also extended or contracted. In the aforementioned figure material surfaces are sketched starting from a surface arbitrarily fixed at the point t_0. In theory a material surface cannot became discontinuous even if in practice its detection can be subject to the limits already discussed in conjunction with the interface. Surface stretching is defined as the temporary evolution of the surface area [3]. The stretch ratio, or SR, is the ratio between the material surface area at time t and the area at time t_0, for which

$$\mathrm{SR} = \frac{\delta \mathrm{A(t)}}{\delta \mathrm{A(t_0)}} \tag{2-4}$$

The stretch rate $K_{\delta A}$ is the relative change of the stretch ratio, SR

$$K_{\delta A} = \frac{D}{Dt} \ln SR \tag{2-5}$$

The surface stretch rate is linked to the velocity pattern of the flow, in which it evolves, by the following kinematic relationship:

$$K_{\delta A} = \boldsymbol{\nabla} \cdot \boldsymbol{V} - \boldsymbol{\nabla}\mathbf{V} : \mathbf{nn} \tag{2-6}$$

where $\mathbf{n}$ and $\boldsymbol{V}$ are the normal unit vector and the velocity vector of the surface δA, respectively. This expression can be read in an heuristic way as the difference between a volumetric stretch, $K_{\delta \mathcal{V}}$, and a linear one, $K_{\delta l}$, bearing in mind that the stretch rate is additive by virtue of its logarithmic nature. The definitions of volumetric $K_{\delta \mathcal{V}}$ and linear $K_{\delta l}$ stretch rates and their kinematic expressions are given below for completeness

$$K_{\delta V} = \frac{1}{\delta \mathcal{V}(t_0)} \frac{D}{Dt} \delta \mathcal{V}(t) = \boldsymbol{\nabla} \cdot \boldsymbol{V} \tag{2-7}$$

$$K_{\delta l} = \frac{1}{\delta l(t_0)} \frac{D}{Dt} \delta l(t) = \boldsymbol{\nabla}\mathbf{V} : \mathbf{nn} \tag{2-8}$$

It is also possible to demonstrate [3] that

$$K_{\delta A} = \boldsymbol{\nabla}_t \cdot \mathbf{V}_t + \mathrm{V}_n C \tag{2-9}$$

where $\mathbf{V}_t$ and V_n are the projection of the velocity vector $\boldsymbol{V}$ on the surface δA and the modulus of the projection $\mathbf{V}_n$ along the normal to the surface, respectively, $\boldsymbol{\nabla}_t$ the divergence operator on the surface δA and $C = \boldsymbol{\nabla} \cdot \boldsymbol{n}$ its curvature. This last expression shows that the stretch rate consists both of a contribution related to the "planar divergence" of velocities on the surface and of a contribution related to the surface curvature.

An intermaterial surface is a material surface defined at time t_0 on the interface. In general intermaterial surfaces of practical interest are those partially limited by the first contact point (or line). By first contact point (or line) we mean the point (or line) of the interface through which the tracer passes with the shortest residence time. In a jet, for instance, the first contact line is the border of the jet's exit orifice. In fact all the possible interfaces, obtained by plotting the jet, pass through the side of the jet's orifice at residence time of practically zero. In the opposite jets configuration the first point of contact is the stagnation point.

An example of an intermaterial line is shown in Figure 2.2b. The same lines, used as example of material surface sections on the left side, are shown again together with the interfaces at time t_0 and t_2, sketched as red lines between the seeded (black) and unseeded (white) flows.

2.3.3. Eulerian – Lagrangian surfaces

Interfaces and isosurfaces are here defined "progressive" when they refer to tracers which are injected at the inlet boundary after a fixed reference time, t_0. They are easy to be envisaged from a conceptual view point, but difficult to be evaluated by means of numerical models or experimental techniques.

In the DNS of a planar 2-D flow, given in Figure 2.3a, a species A, which is injected at an average velocity $\boldsymbol{V}_A = 1.4\ m/s$ into an external flow, B, which proceeds with average velocity $\boldsymbol{V}_B = 0.14\ m/s$.

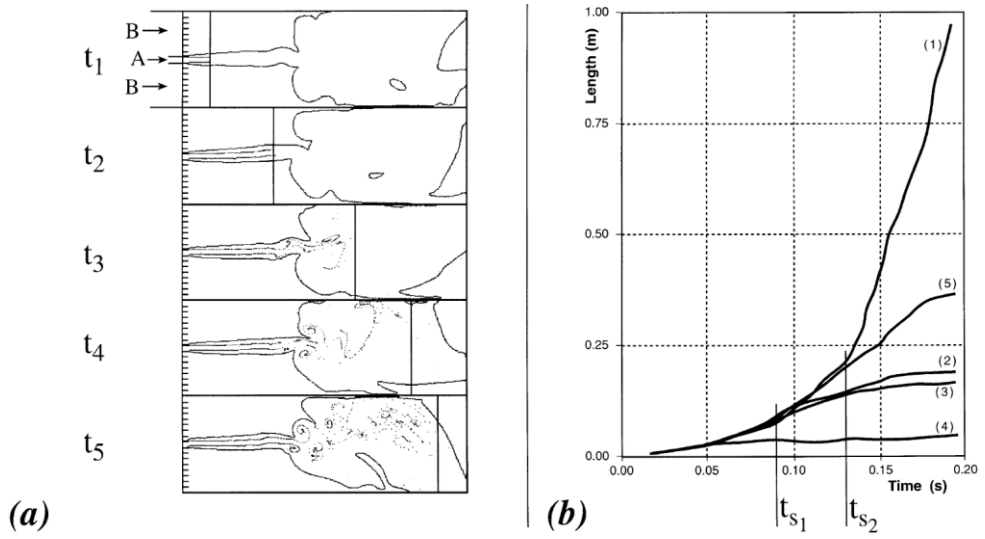

Figure 2.3. (a) Sequence of progressive isosurfaces (solid contour on the left of the vertical lines) and of progressive interfaces (dotted lines). (after Cavaliere 1995). (b) Linear extension of progressive interface (line 1) and isosurfaces (line: 2 at $Z = 0.05$, 3 at $Z = 0.95$, 4 at $Z = 0.5$, 5 at $Z = 0.391$) section versus residence time.

Details, concerning the flow configuration can be found in the original article [9]. The point of interest is that at time t_0 non-diffusive massless particles are injected at the boundary in the rim which separates the two flows and they are convected downstream. The interpolating curve, shown as a solid line, determines the progressive interface at times $t_1 \ldots t_5$.

This surface is Eulerian because it is part of an Eulerian surface, i.e. an interface, and it is Lagrangian because it is bounded on one side by the tracer which is injected at time t_0 and which proceeds towards the outlet. This border line (or point, as in the 2-D example) can be defined as "leading line" (or point)

at a generic residence time, t. The progressive interface always increases, with time, by definition, but the increasing rate depends on the stretch to which it is submitted. Its extension, in the example given here, is reported in Figure 2.3b as a function of time with the line tagged "1".

The progressive isosurfaces of the example reported in Figure 2.3a can be approximated by the part of isosurfaces, which are upstream of the leading point of the flows, i.e. on the left side of the thick line which crosses this point perpendicularly to the main flows direction. They refer to a fixed mixture fraction, approximately corresponding to the stoichiometric value of a large paraffin − air flame, i.e. $Z = 0.05$. This is a relevant value, because it refers to a mixture fraction in the peripheral part of the mixing layer. The extension of the progressive isosurface with time is reported in Figure 2.3b as line "2". This overlaps the progressive interface up to time t_{s_1} showing that the extension of the two surfaces is identical. It then increases at a slower rate for reasons that will be clarified below. One of this consists in the fact that progressive isosurface may undergo an annihilation process when two parts of it merge into each other.

Curve "3", "4" and "5" (referred to progressive isosurface at mixture fraction $Z = 0.95$, $Z = 0.5$ and $Z = 0.38$) show similar behavior with respect to that relative to $Z = 0.05$ with different splitting time at which they separate from the progressive interface. The splitting time of the surface at $Z = 0.38$ is also marked on the abscissa with t_{s_2} because of its relevance in mixing classification, which will be presented in Chapter 5.

Progressive interface and isosurface are quantities, which only recently have been defined, and their experimental evaluation is not extensively documented. However, it is clear that the difficulty in their measurement lies in their Lagrangian nature. In fact, the detection feasibility of the progressive isosurface depends on the possibility of injecting non-diffusive and diffusive tracers

starting from the arbitrary time t_0. This is a difficult task if the transition, from absence to presence of tracer, has to be ensured at the same time on the whole inlet boundary. Furthermore, the tracer injection at the inflow boundary can interfere with fluid-dynamic inlet conditions and it cannot be anticipated upstream of the boundary without pre-stirring or pre-mixing the traced and non-traced flows. Techniques based on smoke wire devices or on photochromic tracers, that change their physical/optical properties when crossing a light sheet on the boundary, are possible candidates to generate identifiable progressive interfaces and isosurfaces.

2.3.4. Surface evolution

It is possible to define various important quantities, that results very useful for the theoretical description of material surfaces [12]. Surface weighted value $Q_{\Delta A}$ of whatever quantity is defined according to Equation 2-10 with respect to a generic surface ΔA:

$$Q_{\Delta A} = \frac{\iint_{\Delta A} Q dA}{\Delta A} \tag{2-10}$$

$$Q|_{\Delta A} = \iint_{\Delta A} dQ \tag{2-11}$$

where $Q|_{\Delta A}$ is the local value of the quantity Q with respect to the surface ΔA.

Moreover, ensemble average quantities $\hat{Q}$ are defined in the Equation 2-12, as the expected value of $Q_{\Delta A}$

$$\hat{Q} = \langle Q_{\Delta A} \rangle = \langle \iint_{\Delta A} Q dA \rangle \frac{1}{\langle \Delta A \rangle} \tag{2-12}$$

Similarly to surface weighted value, is possible to define respectively volume weighted average ($Q_{\Delta A}$), local ($Q|_{\Delta A}$) and ensemble quantities ($\tilde{Q}$).

$$Q_{\Delta V} = \frac{\iiint_{\Delta V} Q dV}{\Delta V} \tag{2-13}$$

$$Q|_{\Delta V} = \iiint_{\Delta V} dQ \tag{2-14}$$

$$\tilde{Q} = \langle Q_{\Delta V} \rangle = \langle \iiint_{\Delta V} Q dV \rangle \frac{1}{\langle \Delta V \rangle} \tag{2-15}$$

The local surface-to-volume ratio σ is defined as the ratio between the infinitesimal surface area dA with respect to the infinitesimal volume $d\mathcal{V}$.

$$\sigma = \lim_{\Delta V \to 0} \frac{\Delta A}{\Delta V} = \frac{dA}{dV} \tag{2-16}$$

The volume-average of $\sigma_{\Delta V}$ is defined in Equation (2-17).

$$\sigma_{\Delta V} = \frac{\iiint_{\Delta V} \sigma dV}{\Delta V} = \frac{\iiint_{\Delta V} \frac{dA}{dV} dV}{\Delta V} = \frac{\iiint_{\Delta V} dA}{\Delta V} = \frac{A|_{\Delta V}}{\Delta V} \tag{2-17}$$

The expected value of $\sigma_{\Delta V}$, at fixed Eulerian position, is here named as "interface density" (Σ) and it is defined by Equation (2-18).

$$\Sigma = \left\langle \sigma_{\Delta V} \right\rangle = \left\langle \frac{A|_{\Delta V}}{\Delta V} \right\rangle = \frac{\langle A|_{\Delta V} \rangle}{\Delta V} = \tilde{\sigma} \tag{2-18}$$

It is important to underline that interface density Σ is conceptually different from the flame surface density $\Sigma|_Z$ firstly Z introduced for the coherent flame model [13] and then identified by other authors [14], with the stoichiometric iso-surface $Z = Z_{st}$.

A physical interpretation of Σ, is that its inverse is a striation thickness [15]. The striation thickness is related to the amount of area between the fluids

[16]. This quantity can be interpreted as a structured continuum property; thus, if the surface is multiply folded so that locally it appears like parallel planes (i.e. the structure is lamellar and uniform), then the mean distance between the planes is Σ^{-1}. This quantity is useful in describing mixing with diffusion and reaction [17].

Interfaces are determined by means of a non-diffusive tracer that is introduced into part of the flow. With respect to this fact, a local tracer volume fraction is defined is defined by Equation (2-19) as the local ratio of a non-diffusive tracer volume $d\mathcal{V}_{Tr}$ with respect to the infinitesimal volume considered $d\mathcal{V}$:

$$\varphi = \lim_{\Delta V \to 0} \frac{\Delta V_{Tr}}{\Delta V} = \frac{dV_{Tr}}{dV} \tag{2-19}$$

Analogously to interface density; also for the tracer volume fraction is possible to define respectively volume averaged ($\varphi_{\Delta\mathcal{V}}$) and ensemble quantities (Φ):

$$\varphi_{\Delta V} = \frac{\iiint_{\Delta V} \varphi \, dV}{\Delta V} = \frac{\iiint_{\Delta V} \frac{dV_{Tr}}{dV} dV}{\Delta V} = \frac{\iiint_{\Delta V} dV_{Tr}}{\Delta V} = \frac{V_{Tr}|_{\Delta V}}{\Delta V} \tag{2-20}$$

$$\Phi = \left\langle \varphi_{\Delta V} \right\rangle = \left\langle \frac{V_{Tr}|_{\Delta V}}{\Delta V} \right\rangle = \frac{\left\langle V_{Tr}|_{\Delta V} \right\rangle}{\Delta V} = \tilde{\varphi} \tag{2-21}$$

It is worth noting that the volume fraction Φ is directly related to the concentration of the tracer in the considered volume. In particular, a unit value of Φ would correspond to a cell full of tracer, while a zero value would indicate that the cell contained no tracer.

Finally, it is possible to define a characteristic length for the stirring process (ψ), as the inverse of the ratio between the quantities previously defined:

$$\psi = \left(\frac{\sigma}{\varphi} \right)^{-1} \tag{2-22}$$

Analogously to interface density and volume fraction; also for ψ is possible to define respectively volume averaged ($\psi_{\Delta V}$) and ensemble quantities (Ψ):

$$\psi_{\Delta V} = \left(\frac{\sigma_{\Delta V}}{\phi_{\Delta V}} \right)^{-1} \tag{2-23}$$

$$\Psi = \left\langle \psi_{\Delta V} \right\rangle = \tilde{\psi} \tag{2-24}$$

Ψ is named here as "interface extension" and represent a measure of the mean thickness of the interface. This quantity allows to unify, in a fascinating way, concepts on mixing and atomization. In fact, the interface extension is a sort of analogous of the Sauter mean diameter for the atomization process [18].

Chapter 3

Methodological approaches

3.1. Experimental approach

The main features of a model experiment, which should keep the main characteristics of a turbulent mixing pattern, are the following:

- Low dimensionality; i.e. the final target of a quasi-2-D, time dependent fluid-dynamic pattern.
- Small range of length scales of fluid-dynamic structures; i.e. low Re so that the fluid-dynamic pattern can be described both by full numerical simulation and 2-D imaging.
- Perturbation of the pattern that should be able to generate high level of velocity gradient.

This latter requirement conflicts with the second one. In fact high velocity gradients related to high level of vorticity imply large velocity scales, whereas low Re requires low value of velocity. A possible way of satisfying both conditions is the superimposition of a strong perturbation with small-length scales on fluid-dynamic pattern. Also the perturbation has to be quasi-2-D and space-periodic in order to keep the advantage obtained by the dimensional reduction. An experimental apparatus, sketched in Figure 3.1, has been designed with the purpose to satisfy the aforementioned conditions. The test rig used in this work was built to reproduce the stirring/mixing characteristics of gaseous jets under the perspective of the theoretical analysis of the problem.

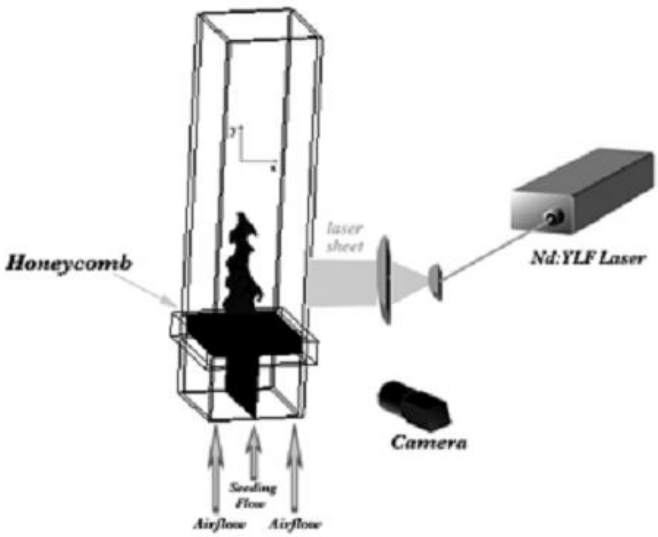

Figure 3.1. Sketch of the experimental apparatus.

The test section of the system is a glass windowed channel with $140 \times 128\, mm$ cross-section, designed to operate at atmospheric pressure and environmental temperature conditions.

In order to face the difficulty previously mentioned, the first requirement of the experimental flow to be investigated was fulfilled by choosing a flow configuration which is 3-D planar symmetric. The feeding system of the gaseous flows was designed in order to achieve both a high degree of turbulence level control and repeatability of inlet conditions. Design process has been strongly guided by feasibility criteria [12]. In addition, the design of the mixing test was such that both the building of the experimental apparatus and the numerical simulations were possible and meaningful. In this respect the most important features were considered to be the turbulent and 3-D character of the flow, as well as the choice of well defined, stable and easy to implement boundary conditions. A further characteristic, i.e. the spatial periodicity of the flow, is quite desirable in a numerical simulation of the fluid-dynamic pattern. A honeycomb (reported in Figure 3.2), formed by square channels with a cell size

of $2\,mm$, is used to obtain the desired fluid dynamics conditions in the test section.

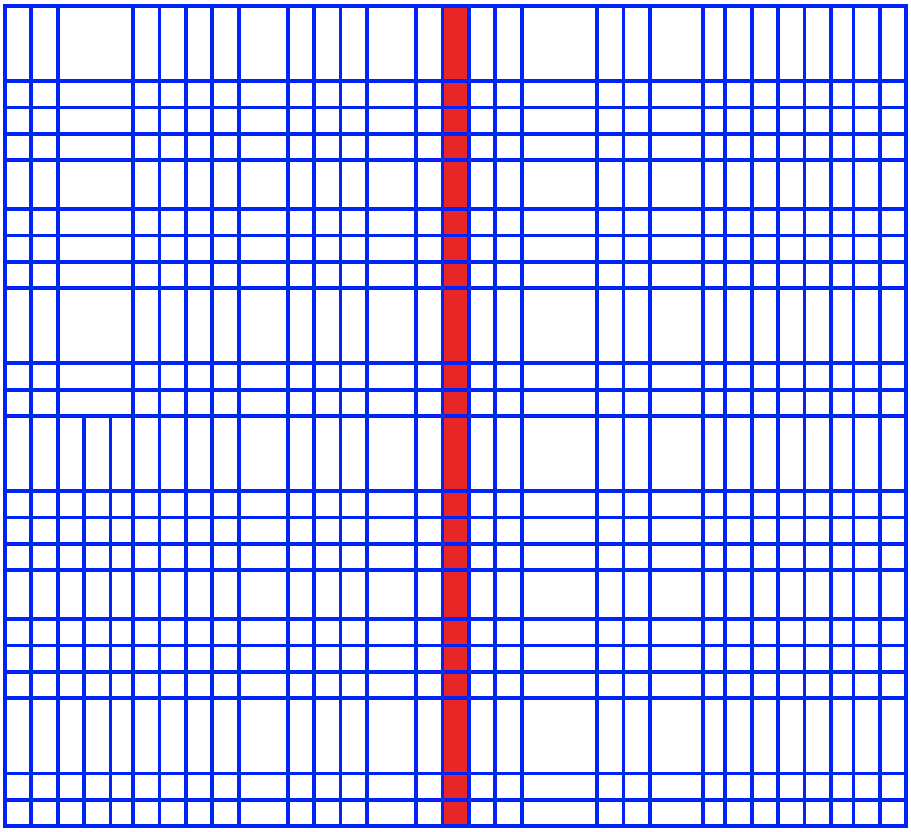

Figure 3.2. Details of the feeding configuration.

This structure has 35 channels along the x-direction and 32 channels in the other one. Therefore, the cross section of the test duct has a very large aspect ratio (10). The length of any duct ($30\,mm$) is much larger than its width ($H \gg L$) so that self-similar velocity profiles can develop. Furthermore the duct widths are small enough to ensure that, for the employed average velocities, relatively low Re are obtained and laminar Poiseuille-type flows can be reasonably supposed to develop in every duct of the honeycomb structure. This means that natural boundary conditions are used. Moreover, the fact that the

cross section of the test duct has a very large aspect ratio ($L^* \gg L$ as reported in Figure 3.3) permits to have transitional/turbulent flow conditions in the main test chamber.

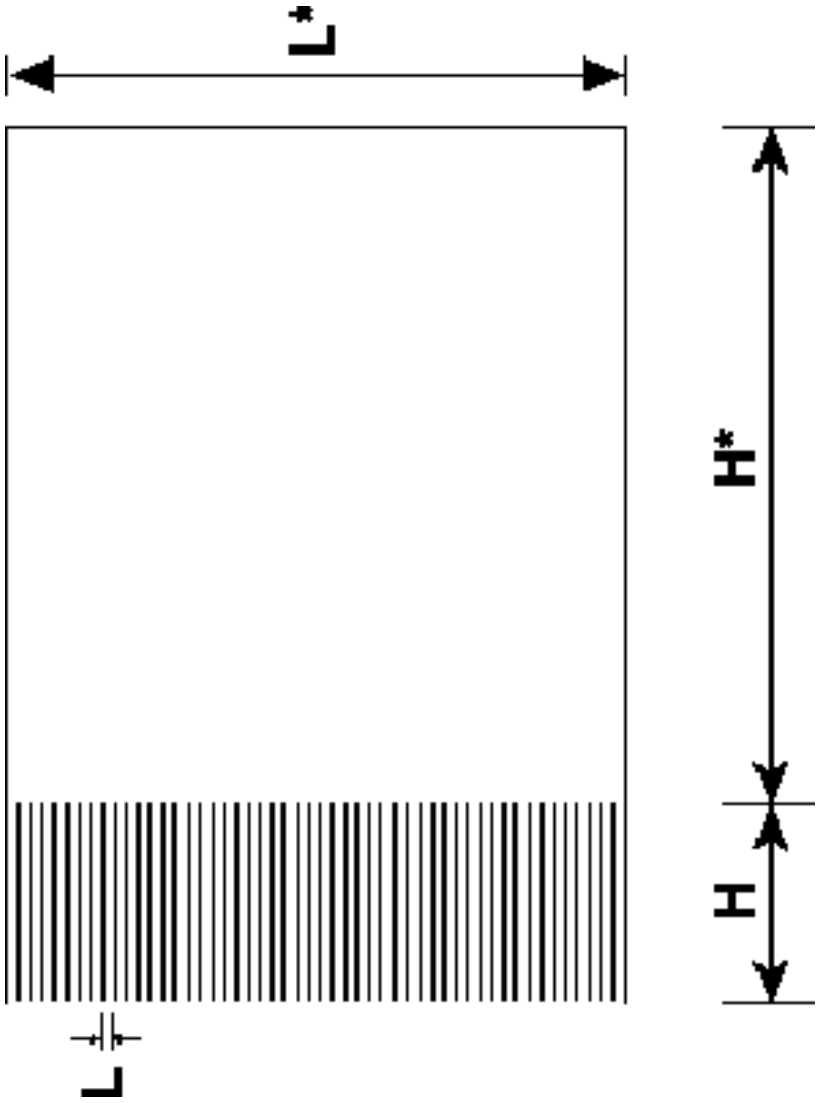

Figure 3.3. Frontal view of the chamber.

Finally, in order to control the streak-lines roll-up process, the ducts in the central row of the honeycomb structure are independently fed with a seeding

flow and the airflow velocity can be varied independently from the velocity in the other ducts.

Special care is devoted to assure an even distribution through the remaining ducts. The test section of the experiment is a rectangular channel, made of optical grade glass in order to have optical accessibility on all the four sides (see Figure 3.1).

In order to analyze the stirring characteristics, interfaces from two flows have been generated by means of some devices later described. In this case, the diagnostics problem is the same [19].

It consists of detecting the concentration of some tracers, which could be submicron particles produced by various types of methods.

For this reason, the generation of the interface is obtained by seeding the central part of the flow with submicron particles. The seeding particles are illuminated by a laser light sheet perpendicularly crossing the test chamber allowing for interface identification as the discontinuity in the 2-D laser light scattering intensity due to the discontinuity of the tracer concentration.

It is worthwhile to note, that the type of particles, for which $Sc \gg 1$ and $Stk \ll 1$, is the only possible choice of tracer in a gaseous system [4]. A particle, for instance, between 0.1 and $1\ \mu m$ is sufficiently large in dimension to ensure that Brownian diffusion is low, but it is sufficiently small to immediately follow a flow.

Moreover, intensity of the scattered light, as a direct measure of particle size has always been plagued with difficulties, as detected intensity is dependent on so many other parameters of a flow system (e.g., trajectory of particle through a shaped beam/sheet, obscuration of incident and scattered light, extinction), despite some early attempts to remove the necessity of calibration [20]. There is also the basic difficulty that, in the Mie scattering range, the intensity is not monotonically dependent on particle size.

For the previous reasons, the central gaseous flow was seeded with TiO_2 particles with a mean diameter of $2\,\mu m$, that correspond to an optimum between the not-diffusing tracer condition and an acceptable scattered light intensity.

In this work it has been chosen to disperse the particles in the airflow by means of an ad-hoc realized elutriator based on a fluidized bed device [21], This solution allowed for the homogeneous dispersion of particles in the airflow and for a satisfying concentration of seeders.

A satisfying characterization of the interface requires the implementation of several on-line diagnostic systems.

The optical characterization of the surfaces is performed by recording the pattern of the light elastically scattered when a laser sheet illuminates the tracer. The Nd:YLF pulsed laser was tuned on the second harmonic wavelength ($\lambda = 527\,nm$) and its beam was shaped by a set of cylindrical lenses to a sheet of constant thickness. It was varied in height by the extension of the objective field. Patterns of elastic scattered light was detected by a CMOS camera with a variable-focus telescope. Since each pulse is in a different frame, there is no directional ambiguity for the velocity vectors. The time and space scales were limited by the laser thickness and the tracer production time and therefore are not sufficient for measuring any range of length scales. Nevertheless, they are smaller than interface separation distances and the residence time needed to characterize the prototypal flows presented here. A shadow-graphic scheme has been adopted to collect images of the jets, with a proper system of lens. The pulsed laser frequency is $1000\,Hz$, the digital camera acquire $8-bit\ 1280 \times 1024\,pixel$ frames at $1000\,Hz$, and a BNC delay generator has been used for time base generation and synchronization. For each test condition a set of 3000 frames has been collected.

The diagnostic apparatus mainly consists of three units:

- Laser LDY Nd:YLF double head, ($\lambda = 527\,nm$), maximal frequency of $10\,kHz$ and output Energy (at $1\,kHz$ and at $527\,nm$ per laser head per pulse) of $15\,mJ$.
- Camera NanoSense MkIII. Maximal resolution $1280 \times 1024\,pixels$. Maximal frame rate $= 2\,kHz$.
- A BNC 575 delay generator that manage the time base generation and synchronization between the devices.

The use of a laser sheet source (Nd:YLF Laser), already available in the laboratory, allow collecting shadowgraph of the turbulent flow, and so a more detailed description of interface behavior should be achieved.

A 2-D double-pulse PIV system with cross-correlation estimation, which was manufactured by Dantec Dynamics, is used for the instantaneous measurements of velocity field. The PIV system consists of the aforementioned laser (Litron Lasers LDY302), software Dynamics Studio 3.14, a high-speed camera with a $105\,mm$ Nikon standard lens, a synchronizing timing hub, and a personal computer for data acquisition.

As said previously, the central flow is seeded with neutrally buoyant TiO_2 particles of nominal mean diameter $2\,\mu m$. Based on a bulk average velocity of $2\,m/s$ (model scale) the Stokes number for these particles is $Stk = 7 \times 10^{-4}$, ensuring accurate flow tracing. Since each pulse is in a different frame, there is no directional ambiguity for the velocity vectors.

Turbulence statistics are computed using 3000 frames to assure the statistically stationary results. Reliabilities of PIV measurements are estimated to be 1.4% and 6% for mean and root-mean-squared (rms) fluctuating velocities, respectively, through the repeated experiments. The particle density in the working fluid is set to give an average of 12 particle images in each

$32 \times 32\ pixel$ interrogation window. Images for PIV were acquired at a rate of $1\ kHz$ and the digitized images are cross-correlated using a recursive rectangular grid algorithm, which uses 32×32 and then 16×16 interrogation windows to find the mean pixel displacement. A Gaussian peak fit is used to determine the location of the cross-correlation peak to sub-pixel accuracy. Post-processing comprises a standard deviation filter to remove spurious vectors, followed by an interpolation to fill any empty locations and a Gaussian smoothing. All measurements reported in this article were made on the mid-plane of section.

The flow field was investigated in the regions downstream of the test-section inlet. The y-coordinate is aligned with the main flow direction.

Spatial averaging across the light sheet thickness is intrinsic to PIV, and consequently the thickness of the light sheet is a limit on spatial resolution in measurement of 3-D flows.

Flow visualizations and PIV measurements have been conducted under various conditions, which differ only for the seeding flow velocity. In these conditions, the flow is rapidly accelerated from laminar state to a transitional flow.

3.2. Numerical approach

As stated above the purpose is to simulate air flowing in a 2-D channel at $\overline{Re} = 2800$, the channel being $10\ cm$ in length and $8.44\ cm$ in width, the specifications of the channel previously investigated by Giancarlo Sorrentino [22]. The DNS simulation will resolve all the scales and individual transitional structures can therefore be identified. There are two different kinds of methods to identify coherent transitional structures (eddies): Eulerian and Lagrangian. However, there is no universally accepted method of identifying a coherent structure [23,24]. The drawback of the Eulerian methods is that they are not

independent of the reference frame, i.e. they are not objective, and as [24] also point out, they require the user to effectively chose the thresholds discretionally. To solve the problem of frame independence Lagrangian methods utilizes particle tracks of tracer particles in order to identify Lagrangian coherent structures (LCS). The MATLAB program should be able to identify LCS and or identify particles belonging to the same injection. Simulation will be performed with the ANSYS computational fluid dynamics (CFD) software FLUENT. Furthermore, the large amount of data generated by DNS will be analyzed and visualized with MATLAB and ANSYS FLUENT.

3.2.1. Basic Fluid Flow Modeling

In [25] a valuable distinction between *modeling* and *simulating* equations is made. When modeling a system of equations, the equations are solved for some mean or average quantity, say the mean velocity $\langle V_i \rangle$ defined as time average [26] at some point $\boldsymbol{x}$

$$\langle V_i \rangle(\boldsymbol{x}) = \frac{1}{T}\int_{-T/2}^{T/2} V_i(t, \boldsymbol{x})\, dt \tag{3-1}$$

where V_i is the instantaneous velocity, $\boldsymbol{x}$ is the spatial dimension, t is the time and T is the averaging time. In order for the time average to be valid the averaging time must be of appropriate length, i.e. much larger than the time scale of the fluctuating velocity field and much smaller than the characteristic time scale of the large scale flow. On the other hand, a simulation of a system of equations means that the instantaneous velocity field is solved directly.

As the intended study is of phenomena occurring during very short time scales, i.e. interactions with single eddies, the solving of average properties will not suffice. Therefore we will have to look at simulation techniques. The choice thus breaks down to basically two options: Direct Numerical Simulation (DNS)

and Large Eddy Simulation (LES) [25,26,27]. The main difference between DNS and LES is that the former simulates all scales while the latter models the smaller scales and simulates the intermediate and large scales. Because conservation equations for mass and momentum perfectly describe laminar flow in an inertial (non-accelerating) reference frame and DNS computes these directly, all scales of $\boldsymbol{x}$ as well as the time scales are calculated and resolved [25,27]. This, together with the huge amount of high resolution data generated, but with large computational demand, makes DNS an attractive choice. The computational cost of DNS is proportional to Re^3 [25,27], however, 99% of the demand is devoted to the dissipation range [25]. The dissipation range length scale l_0 is according to [27] sixty times the Kolmogorov length scale $\eta = (\nu^3/\varepsilon)^{1/4}$, where ν is the kinematic viscosity and ε is the turbulent kinetic energy dissipation rate.

In the next two sections the mass conservation equation and the momentum conservation equations are presented.

3.2.1.1. The Mass Conservation Equation

The equation for conservation of mass, or continuity equation, can be written as follows:

$$\frac{\partial \rho}{\partial t} + \boldsymbol{\nabla} \cdot (\rho \boldsymbol{V}) = 0 \qquad (3\text{-}2)$$

Equation 3-2 is the general form of the mass conservation equation and is valid for incompressible as well as compressible flows.

3.2.1.2. Momentum Conservation Equations

Conservation of momentum in an inertial (non-accelerating) reference frame is described by [28]

$$\frac{\partial}{\partial t}(\rho \boldsymbol{V}) + \boldsymbol{\nabla} \cdot (\rho \boldsymbol{V}\boldsymbol{V}) = -\boldsymbol{\nabla} p + \boldsymbol{\nabla} \cdot (\bar{\bar{\boldsymbol{\tau}}}) \tag{3-3}$$

where p is the static pressure and $\bar{\bar{\boldsymbol{\tau}}}$ is the stress tensor (described below), respectively. The stress tensor $\bar{\bar{\boldsymbol{\tau}}}$ is given by

$$\bar{\bar{\boldsymbol{\tau}}} = \mu \left[(\boldsymbol{\nabla V} + \boldsymbol{\nabla V}^T) - \frac{2}{3} \boldsymbol{\nabla} \cdot (\boldsymbol{VI}) \right] \tag{3-4}$$

where μ is the molecular viscosity, $\boldsymbol{I}$ is the unit tensor, and the second term on the right hand side is the effect of volume dilation.

3.2.2. Modeling Discrete Phase

After solving transport equations for the continuous phase with ANSYS FLUENT, the solution of the CFD computations will be exported as large files of data at discrete points in time and space containing velocities to be read into MATLAB, where a script created to calculate or integrate scalar values along the particle trajectory, allows to simulate a discrete second phase in a Lagrangian frame of reference.

3.2.2.1. Solution Strategies for the Discrete Phase

The underlying physics of the Discrete Phase Model (DPM) is described by Ordinary Differential Equations (ODE) as opposed to the continuous flow which is expressed in the form of Partial Differential Equations (PDE). Therefore, the DPM uses its own numerical mechanisms and discretization schemes, which are completely different from other numerics used in ANSYS FLUENT. Particle tracking is related to an absolute reference frame, which coincides with that of the continuous phase. All particle coordinates and velocities are then computed in this frame, but being this second phase made

up of massless particles dispersed in the continuous phase, the DPM computes the trajectories of these discrete phase entities in the absence of coupling between the phases. The accuracy of the discrete phase calculation thus depends only on the time accuracy of the integration.

The trajectories of the discrete phase injections are computed without impacting the continuous phase (termed an uncoupled calculation). For the uncoupled calculation, you will perform the following two steps:

1. Solve the continuous phase flow field.
2. Compute (and report) the particle trajectories for discrete phase injections of interest.

In an uncoupled approach, this two-step procedure completes the modeling effort, as illustrated in Figure 3.4.

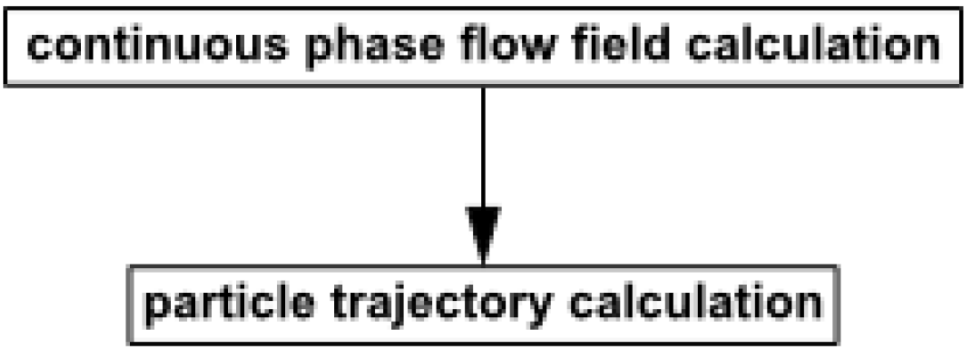

Figure 3.4. Uncoupled Discrete Phase Calculations.

3.2.2.2. Limitations

The procedure described in the previous section is adequate when the discrete phase is present at a low mass and momentum loading, in which case the continuous phase is not impacted by the presence of the discrete phase. That is, the discrete phase formulation used by the DPM contains the assumption

that the second phase is sufficiently dilute that particle-particle interactions and the effects of the particle volume fraction on the gas phase are negligible. In practice, these issues imply that the discrete phase must be present at a fairly low volume fraction, usually less than 10-12%.

The unsteady-particle discrete phase model is suited for flows in which particle streams are injected into a continuous phase flow with a well-defined entrance and exit condition. The Lagrangian model does not effectively model flows in which particles are suspended indefinitely in the continuum, as occurs in solid suspensions within closed systems such as stirred tanks, mixing vessels, or fluidized beds.

Boundedness of planes is not considered during sampling of particle tracks, which means that all particle tracks crossing the unbounded plane are sampled.

3.2.2.3. Steps of the Discrete Phase Model

The primary inputs that one must provide for the discrete phase calculations are the initial conditions that define the starting positions, velocities, and other parameters for each particle stream. One will define the initial conditions for a particle stream by creating an "injection". The initial conditions provide the starting values for all of the dependent discrete phase variables that describe the instantaneous conditions of an individual massless particle, and, for a single injection, include the following:

- position $(x, y$ coordinates$)$ of the particle

  Set the x and y positions of the injected stream along the Cartesian axes of the problem geometry in the X- and Y-Position fields.

- velocities (u, v) of the particle

Set the x and y components of the stream's initial velocity in the X- and Y-Velocity fields.

- mass flow rate of the particle stream that will follow the trajectory of the individual particle $\dot{m}_p$

- duration of injection

  Set the starting and ending time for the injection in the Start Time and Stop Time fields.

For a massless particle, it will only need to define the position of the injection. The particle injection velocity is set by the solver equal to the velocity of the continuous phase at the injection point. A massless particle is a discrete element that follows the flow of the continuous phase. As it has no mass, it has no associated physical properties, and no force is exerted on it. Particles are injected at specific positions $x_0 = x_p(0)$ inside the domain $[0,0.0844] \times [0,0.1]$ with the same velocity as the fluid at the corresponding position, $u_p(0) = u(x_0, 0)$. The integration time step size used to integrate the equations of motion for the particle is equal to 10^{-5} $[s]$, which coincides with the integration time step used by ANSYS FLUENT to compute the velocity of the continuous phase (u). This means that the flow properties will be regarded as being constant between time steps. These initial conditions, along with inputs defining the duration of the discrete phase, are used to initiate trajectory calculations. The algorithm for advecting particles will then be:

1. Create a structured table for each of the position and velocity components of particles.

2. Load data from a delimited ASCII file for the start time.

3. Because the particles location will typically lie in between mesh grid point, calculate velocity components at particle locations by mean of a deterministic method for multivariate interpolation with a known scattered set of points (Shepard's method).

4. Calculate the new particle locations by adding the product of the length of the time step by the particle velocities at the old location (Euler method). Particle positions will be updated, at the end of each time step, as the solution advances in time.

5. Terminate trajectory calculations at the point where particles impact the "escape" boundary.

6. Perform a linear interpolation injecting a new particle within the range of two successive particles when their distance is greater than a specific measure.

7. The predicted trajectories and the associated intermaterial surfaces can be examined graphically and/or alphanumerically.

8. Load the data file of the next time step and repeat until the final time is reached.

Only the steps related specifically to discrete phase modeling are shown here. The procedure above allows us to obtain different flow maps that will be discussed in the next chapter.

3.2.2.4. Transient Treatment of Particles

The Discrete Phase Model utilizes a Lagrangian approach to derive the equations for the underlying physics which are solved transiently. Since solving unsteady equations for the continuous phase, particles are injected with a Fluid Flow Time Step and will always be tracked in such a way that they coincide with the flow time of the continuous flow solver. This means that the Discrete Phase Model cannot be used in combination with changes in the time step for the continuous equations, as it is done when using adaptive flow time stepping.

Additional inputs are required for each injection. Since Particle Tracking is Unsteady, the injection Start Time and Stop Time must be specified. Changing injection settings during a transient simulation will not affect particles currently released in the domain. At any point during a simulation, you can clear particles that are currently in the domain. At the end of the time step, particles are advanced to their new positions based on the continuous-phase solution. In unsteady-state discrete phase modeling, particles do not interact with each other and are tracked one at a time in the domain.

3.2.2.5. Method to approximate the particle velocity

The interpolation method used to approximate the particle velocity is the *Shepard's method* [29]. The current method is obtained through the CFD and inert-particle-tracing simulation. After getting the velocity field, a finite number of tracers (x_i, y_i) $(i = 1,2,\dots,n)$ are released at the mixer plane under analysis. In steady flow, their trajectories coincide with the streamlines. Shepard's method is a simple form of *Inverse Distance Weighting (IDW)* interpolation. As seen in Figure 3.5, P is the unknown point. The solid circle denotes a preset neighborhood that is centered at P and with a radius r_0.

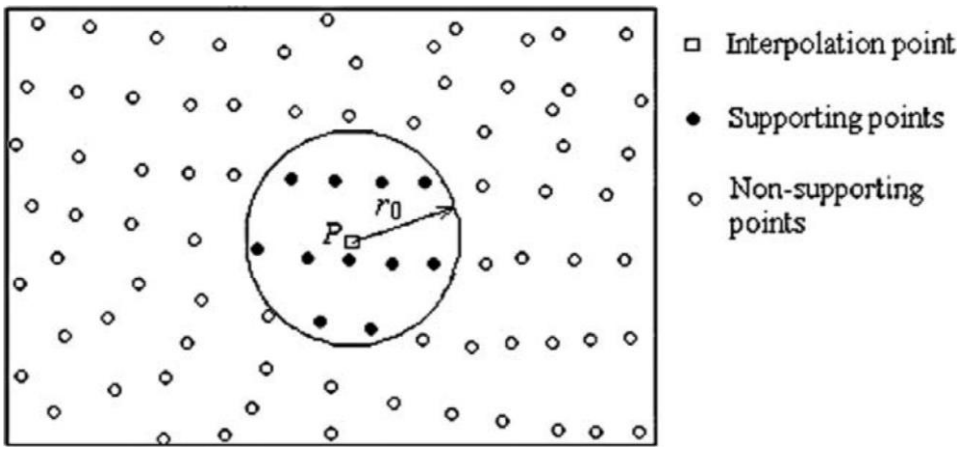

Figure 3.5. Local interpolation using Shepard's method.

The value at P is determined by all the supporting points inside the neighborhood.

$$u_p(x_p, y_p) = \sum_{i=1}^{n} w_i \cdot u(x_i, y_i) \tag{3-5}$$

where $u_p(x_p, y_p)$ is the approximation function, n is the number of supporting points, $u(x_i, y_i)$ $(i = 1, \ldots, n)$ are values of the supporting points, w_i is the interpolation weight,

$$w_i = \frac{r_i^{-p}}{\sum_{i=1}^{n} r_i^{-p}} \tag{3-6}$$

and r_i is the distance from the ith supporting point to the unknown point,

$$r_i = \sqrt{(x_p - x_i)^2 + (y_p - y_i)^2} \tag{3-7}$$

As commonly defined, the weighting exponent p is set as 2. The weight decreases with the increase of r_i: normally, the interpolated value is more influenced by the nodes closer to the interpolation point, then, with the increase of the distance, the influence becomes weaker. Moreover, it has the following two additional properties: (1) it is positive; (2) the summation of the weights for all the supporting points is equal to 1.

The physical equations used for the discrete phase calculations are described in the next sections.

3.2.2.6. Particle Motion Theory

This section describes the theory behind the Lagrangian discrete phase capabilities available in the DPM. Advances in computational fluid mechanics have provided the basis for further insight into the dynamics of multiphase flows. Currently there are two approaches for the numerical calculation of multiphase flows: the Euler-Lagrange approach (discussed in the following section) and the Euler-Euler approach.

The Lagrangian discrete phase model described in this chapter follows the Euler-Lagrange approach. The fluid phase is treated as a continuum by solving the Navier-Stokes equations, while the dispersed phase is solved by tracking a large number of particles through the calculated flow field. The dispersed phase cannot exchange momentum, mass, and energy with the fluid phase.

This approach is made considerably simpler when particle-particle interactions can be neglected, and this requires that the dispersed second phase occupies a low volume fraction, even though high mass loading $\left(\dot{m}_{particles} \geq \dot{m}_{fluid}\right)$ is acceptable. The particle trajectories are computed individually at specified intervals during the fluid phase calculation.

Solution of the discrete phase implies integration over discrete time steps of the equation of motion to yield the particle trajectory. Upon neglecting gravity

and Brownian effects, the equation of motion (for the x direction in Cartesian coordinates) is

$$\frac{dx_p}{dt} = u_p \tag{3-8}$$

which is written in a Lagrangian reference frame. Here, x_p and $u_p = u_p(x_p, t)$ are the position and velocity of the particle, respectively, which, for a massless particle, is equal to the velocity of the carrier flow at the position of the particle. This equation can be solved by analytical integration. The new location x_p^{n+1} can be computed from a similar linear algebraic equation [30]

$$x_p^{n+1} = x_p^n + \Delta t \cdot u_p^n \tag{3-9}$$

where u_p^n represent particle velocities at the old location. Here, we have represented the differential with

$$\frac{dx_p}{dt} \approx \frac{x_p^{n+1} - x_p^n}{\Delta t} \tag{3-10}$$

Thus, we see that the evaluation of the location at the next time t_{n+1} only requires the known location at the instant of time t_n and its derivatives at t_n. Equation 3-9 is applied when using the *Euler method*. It is very efficient because allows sequential solution one at a time, but it can become inaccurate for large steps and in situations where the particles are not in hydrodynamic equilibrium with the continuous flow. Note that Equation 3-9 is basically the Taylor series of x_p^{n+1}

$$x_p^{n+1} = x_p^n + \Delta t \cdot \frac{dx_p^n}{dt} + O(\Delta t^2) \quad (3\text{-}11)$$

where the order symbol O simply means that "left-out" terms have a size magnitude of order Δt^2 (the smaller Δt, the better). Comparing the above Taylor series and Equation 3-9 the analytic discretization scheme has a local truncation error of $O(\Delta t^2)$, with the local truncation error being the error incurred by the approximation over a single step. As time increases, the overall error increases. Since the number of calculations is inversely proportional to the step size, the actual accuracy of the Euler method is $O(\Delta t)$.

3.2.2.7. Boundary Conditions for the Discrete Phase

When a particle reaches a physical boundary (e.g., a wall or outlet boundary) of the geometry, the DPM applies a discrete phase boundary condition to determine the fate of the trajectory at that boundary. The available boundary condition types are

- **reflect**

  The particle rebounds the off the boundary in question with a change in its momentum as defined by the coefficient of restitution (see Figure 3.6).

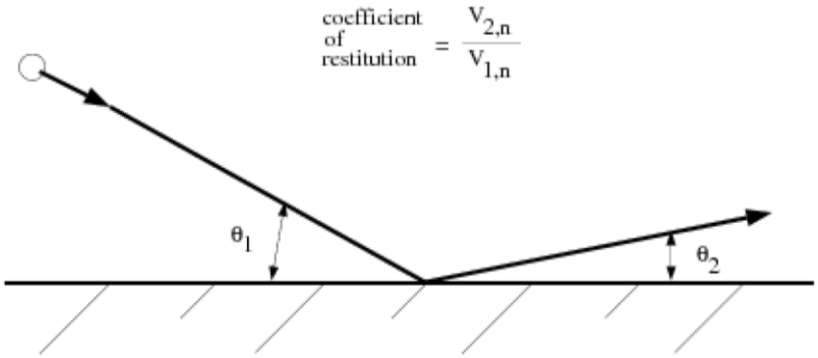

Figure 3.6. "Reflect" Boundary Condition for the Discrete Phase.

The normal coefficient of restitution defines the amount of momentum in the direction normal to the wall that is retained by the particle after the collision with the boundary [31]:

$$e_n = \frac{v_{2,n}}{v_{1,n}} \tag{3-12}$$

where v_n is the particle velocity normal to the wall and the subscripts 1 and 2 refer to before and after collision, respectively. Similarly, the tangential coefficient of restitution, e_t, defines the amount of momentum in the direction tangential to the wall that is retained by the particle.

A normal or tangential coefficient of restitution equal to 1.0 implies that the particle retains all of its normal or tangential momentum after the rebound (an elastic collision). A normal or tangential coefficient of restitution equal to 0.0 implies that the particle retains none of its normal or tangential momentum after the rebound.

Nonconstant coefficients of restitution can be specified for wall zones with the reflect type boundary condition. The coefficients are set as a function of the impact angle, θ_1, in Figure 3.6.

- **escape**

  The particle may escape through the boundary. Trajectory calculations are terminated and the particle is lost at the point where it impacts the boundary (see Figure 3.7).

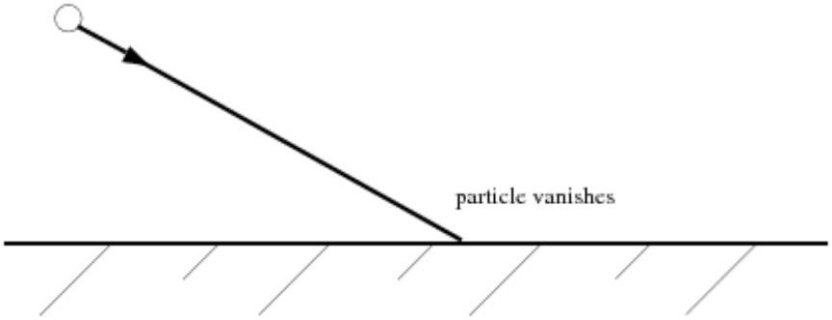

Figure 3.7. "Escape" Boundary Condition for the Discrete Phase.

The DPM makes the following assumptions regarding boundary conditions:

- The reflect type is assumed at wall with both coefficients of restitution equal to 1.0 (all normal and tangential momentum retained).

- The escape type is assumed at all flow boundaries (velocity inlets and outlet).

Chapter 4

Cross-checking of numerical-experimental procedures

4.1. Main results and cross-checking

Some results relative to a reference condition, corresponding to a $\overline{Re} = 2800$ are reported in the following. The $\overline{Re}$ is based on the mean velocity pattern in the chamber.

For this case, profiles of interface density have been obtained and they will be shown in the following with results of main velocity fields and strain rate conditioned on the interface location. The flow visualizations have been performed for seeding-flow velocity of 3.3 m/s while the velocity in the outer channels has been fixed to 0.5 m/s. These values have been chosen to reproduce transitional flow conditions into the test section. The pattern on the left of Figure 4.1 shows instantaneous representative image of the flow inside the test-section, taken in the mid-plane for the reference case.

Figure 4.1. Image of flow inside the chamber with the respective binary and contour images.

The image reported in the figure is only an example and is useful to give an impression of the great variety of structures, which can be established in 3-D flows.

The visualizations have been obtained by means of a 2-D laser sheet technique for detecting the interface. The sequence of consecutive visualizations is taken at a $1\ kHz$ frequency.

It is here useful to underline that behind this representation there is an important hypothesis, namely that for low Re the flow field remains almost 2-D [32] and then it can be characterized by means of a 2-D diagnostic system.

In this sense, the cross-check that will be show below is very useful in assessing the validity of 2-D assumption.

An image processing procedure has been carried out in order to obtain the interface contour, showed in the right of Figure 4.1, which is located where the concentration of the tracer is discontinuous, that is where it passes from zero to a finite value on an infinitely thin surface, and to compute some numerical indicator of the ongoing of the stirring process. The instantaneous interface position is determined from the sharp gradient in the seeding concentration.

In order to obtain an assessment of the experimental results, a comparison with some numerical results is here reported.

A DNS has been performed in FLUENT 6.3 on a simple flat configuration with an adaptive mesh. The geometry consists of a main channel with a ratio $1:1$ of height to length, in which 35 square channels of $2\ mm$ in width compose the inflow boundary. In order to create a relatively unstable flow near the exit of the channels, the seeding-flow is fed in the central one with a velocity approximately 6 times higher than the others ($3.3\ m/s$). The Re in this channel is, however, such as to ensure a laminar initial motion ($Re = 470$). Starting from a fixed time, which is conventionally assumed to be equal to the value zero, the flow is seeded with massless particles at the tip of the rim which separates the central duct with the lateral ducts in correspondence of the first

contact point. The trajectory of the particles is simulated using an Eulerian-Lagrangian approach. In practice the trajectory calculations are performed using the local continuous phase conditions as the particle moves through the flow. The interpolating curve determines the intermaterial line at different times. From this point of view, the interface is defined as a set of particles that have same border of the jet confinements. The isosurfaces are instead related to the solution of the transport equation on a fixed volume control. In this case, a unitary mass fraction is distributed along the points of the input section of the small central channel.

For the flow configuration abovementioned an ensemble of patterns obtained from flow visualizations and numerical computations are reported in Figure 4.2.

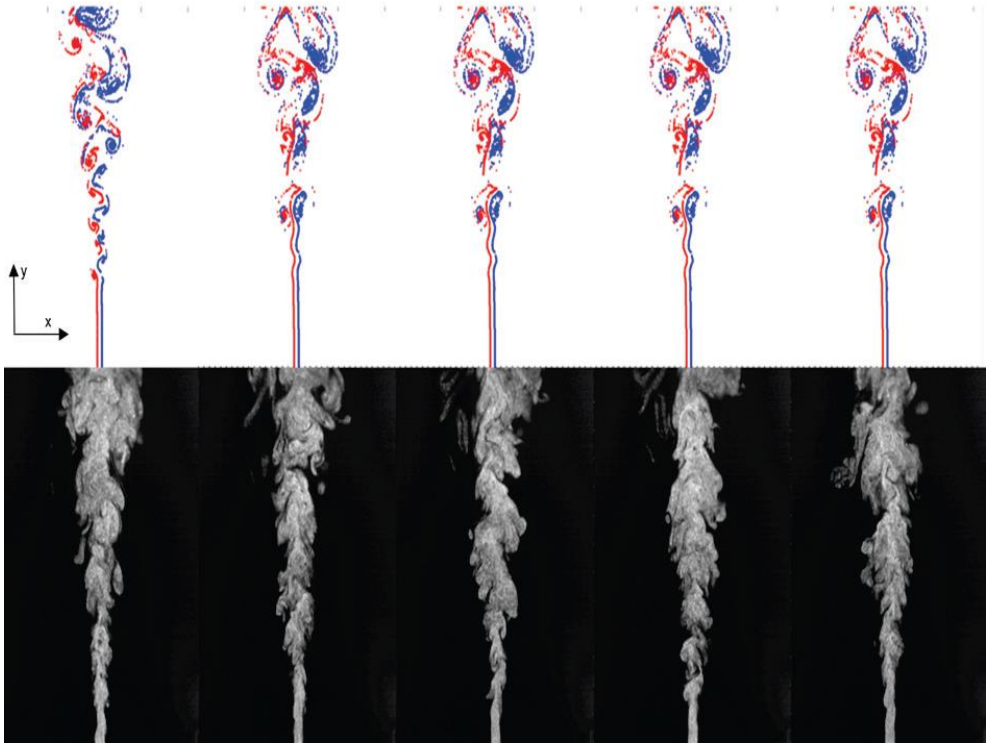

Figure 4.2. Experimental/Numerical comparison of interfaces for a 2-D transitional flow.

Blue particles indicate the right interface contour and red indicates the left one. The upper row is relative to numerical predictions while the lower one is relative to pattern of laser light scattered by a sub-micron seeding. The field of view is $4\,cm \times 10\,cm$. Both numerical and experimental results are reported in Figure 4.2 for five selected times.

It is of great interest to underline that the comparison is quite satisfactory. Among the numerical predictions, the agreements are not so good in the high-convolution zones. Interfaces are quite convoluted, as it is possible to observe in Figure 4.2. They undergo a relatively intense stretch rate. The stretch rate is sufficient for high level of convolution. Moreover, the interface contour at the downstream region in the numerical results is not well identified due to the high stretch rate. In general the agreement are quite satisfactory and they depict an important assessment of the experimental results.

A quantitative experimental/numerical comparison for the patterns reported in Figure 4.2 has been obtained by comparing the mean velocity magnitude profiles conditioned on the interface along the dimensionless axial direction (X/D) for three selected streamwise positions (Y). They are reported in Figure 4.3. The mean velocity magnitude has been obtained by means of ensemble average of the instantaneous velocity fields. The experimental results in Figure 4.3 have been obtained by means of PIV measurements. The computed mean velocities along the interface are also shown in Figure 4.3. The agreement between experimental and numerical results is quite good. For each streamwise position, there are two local maximum in the mean velocity relative to the interface position and an increase in velocity through the interface zone due to the local stretch.

Another quantitative cross-check has been obtained by comparing the ensemble average strain rate profiles conditioned on the interface along the dimensionless axial direction (X/D) for three selected streamwise positions (Y). They are reported in Figure 4.4.

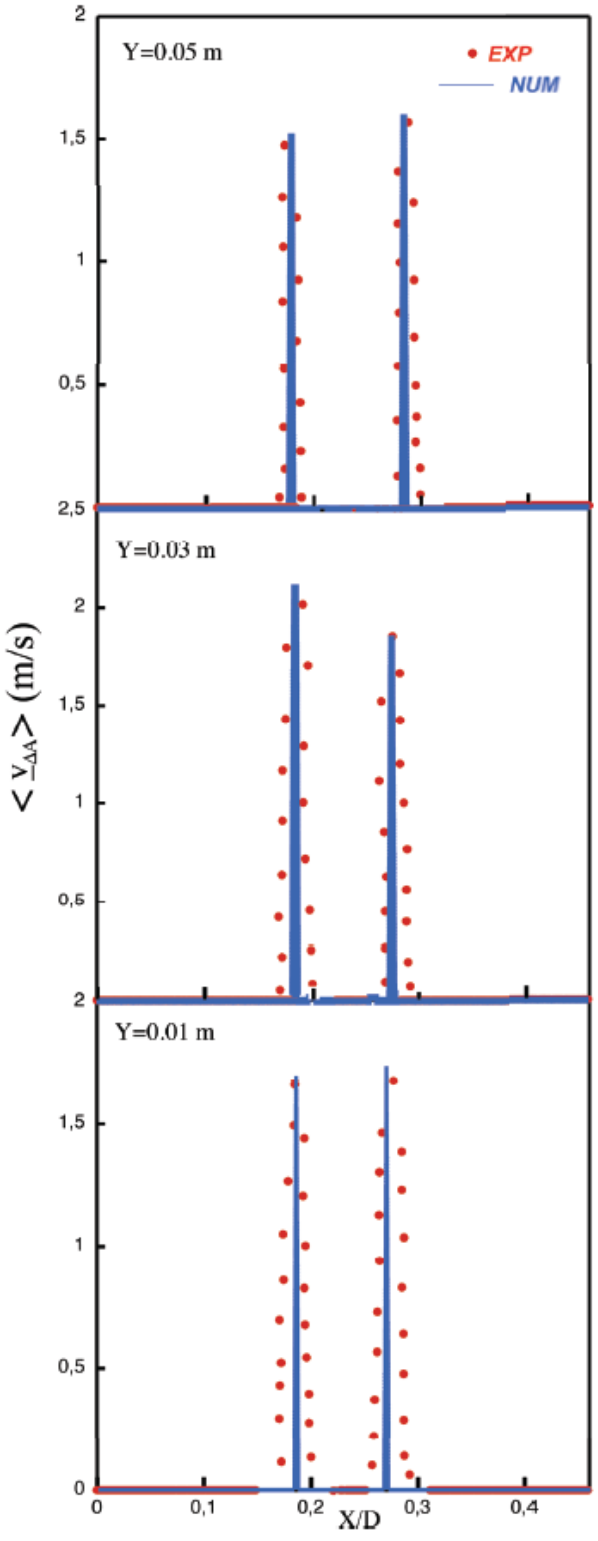

Figure 4.3. Cross-Checking of Experimental/Numerical velocity fields conditioned on interface location.

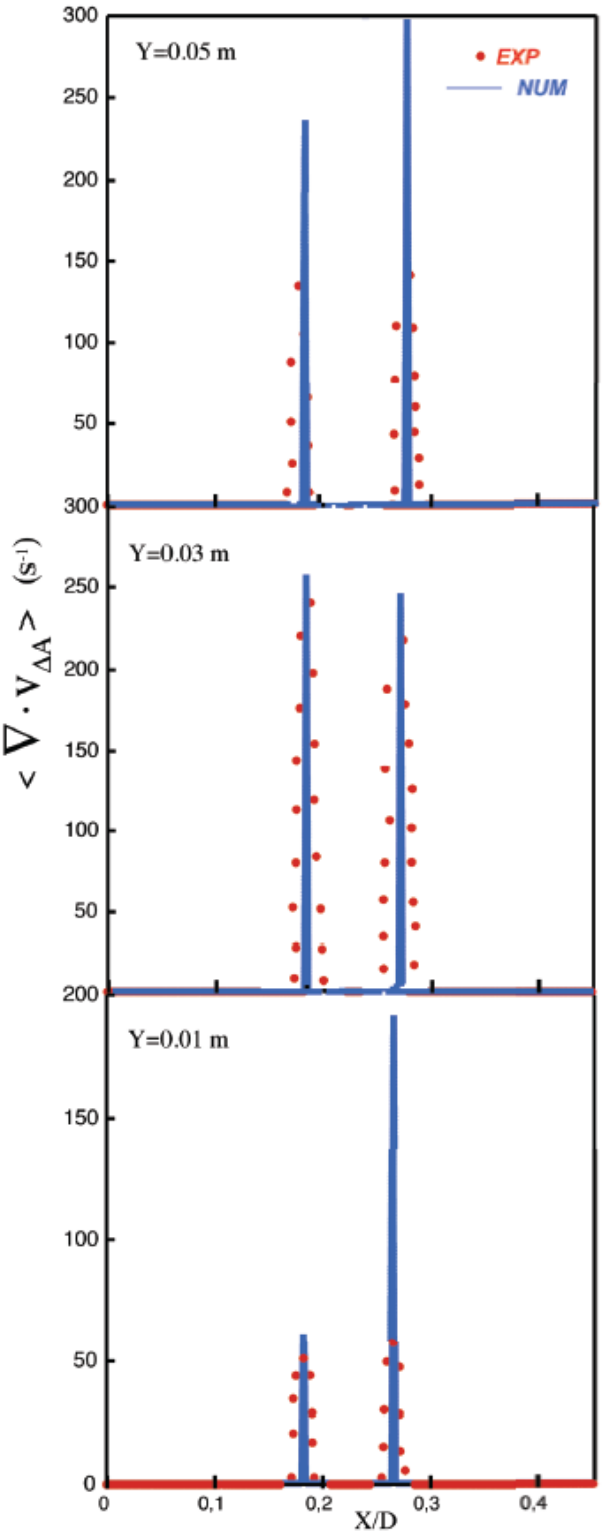

Figure 4.4. Cross-Checking of Experimental/Numerical strain rate conditioned on interface location.

The comparison between experimental and numerical results is quite good only for the central plot at $Y = 0.03\,m$. In this case, the results are qualitatively the same. Moreover, for $Y = 0.01$ and $0.05\,m$ the numerical profiles show a not good quantitative agreement with experiments.

Chapter 5

Results

5.1. 2-D Isothermal characterization of a transitional jet in a co-flow configuration

5.1.1. Intermaterial Surface Visualization and Topology Structure Characterization

As reported in the introduction, one of the aim of this work is the characterization/description and the statistical modeling of diffusive structures evolution (and their mutual interaction) in simple and complex flows. In this section results concerning 2-D isothermal structures evolution related to a transitional jet in a co-flow configuration are presented and discussed.

Figure 5.1 shows the intermaterial surface evolution related to a transitional jet at different simulation times step. Left jet interface is highlighted in red, the right one in blue. First of all, it is worthwhile to note that with the particle tracking procedure developed in this thesis a full detailed characterization of a diffusive structure evolution is achieved. At the first simulation time steps (Figure 5.1a), simple diffusive structures can be detected, together with the onset of a vortex structure formation. At this time, a well-defined vortex structures and a mutual interaction of diffusive structures (there is no a mutual interaction of interfaces) is absent. At higher time steps (Figures 5.1b and 5.1c), as the jet moves forward, well/defined vortex structures can be highlighted. Such a structures grow in number increasing the simulation time, with the interaction between the two inter-faces that becomes stronger. The complexity of a single vortex structure increases with the simulation time, in fact. In fact, a comparison between Figures 5.1b and 5.1c

highlights that the number of convolution of a single vortex structure increases by increasing simulation time.

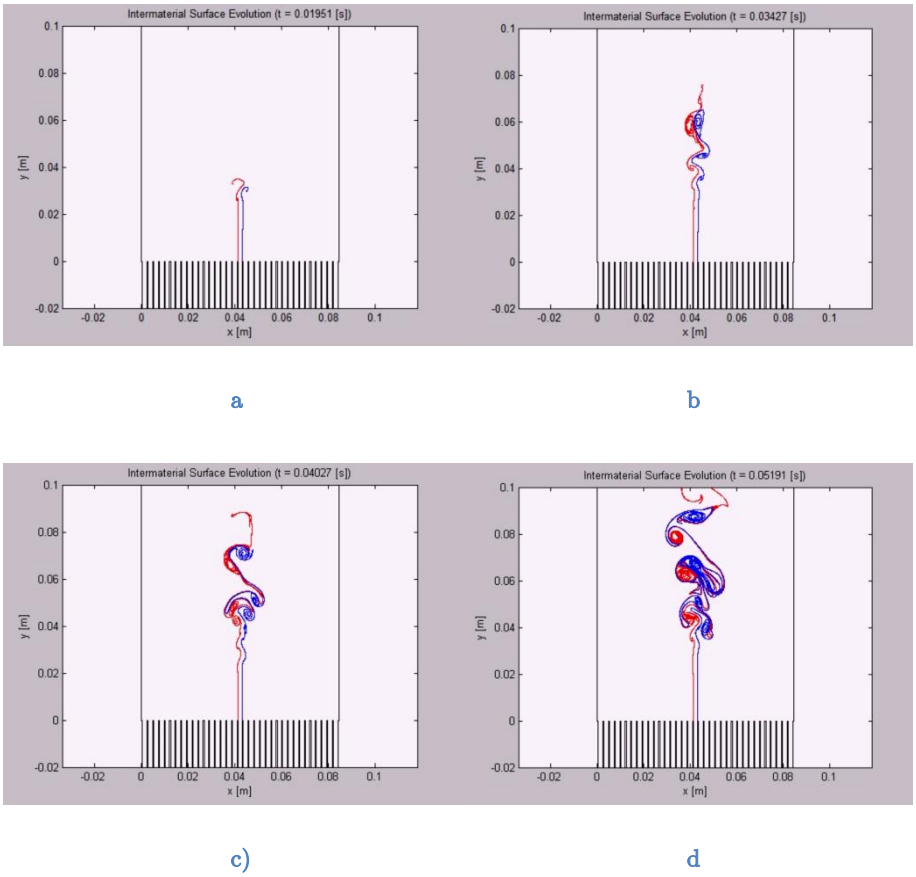

Figure 5.1. Intermaterial surface evolution at different times related to a 2-D transitional jet (from top, clockwise direction).

The alternate shedding of vortices on the left and on the right side is also observable. Here, the main characteristic is that central jet, delimited by interfaces, are embedded inside a vortex structure of the external flow.

Finally, Figure 5.1d shows jet interfaces at the highest simulation time step of that chosen. As it is possible to note, the number of vortex structures increases further. Moreover, structures (and hence, of the jet itself) results bigger (in dimension) with respect to that identified at other time steps

analyzed. Summarizing, the kinematic evolution of an interface has been descripted and it can be schematically portrayed as a sequence of the frames, illustrated in Figure 5.1a-d. In the first frame the roll-up of the protuberance that evolves from the flow is shown accompanied by a curvature of the diffusive layer too. Later on, the single vortex structure starts to convolute. The degree of complexity of the vortex structure, the number of convolution and the intensity of mutual interaction between the two interfaces will be a function of the initial conditions.

It is important to note from Figure 5.1 that a generic isosurfaces and the iso-surface corresponding to the stoichiometric mixture fraction follow the interface contour line between black and white regions) in a parallel way. This behavior makes reasonable to describe this diffusive layer through the 1-D, unsteady, stretched layer [3]. In reality, with respect to this simplified model, different factors come into play such as: interaction between contiguous diffusive mixing layers; distribution of the stretching along the stoichiometric isosurfaces; expansion of gases due to heat release and consequent induced stretch distribution; curvature of isosurfaces. All these factors are effective in different ways according to the initial conditions of the evolution of the vortex or, in other words, according to the thickness of the diffusive layer at the moment when folding begins and they have been taken in account in this work.

In order to reveal more details about the structures detected, the full temporal history of the intermaterial surface, starting from the first simulation time steps to the end of the simulation, is reported in Figure 5.2 for several frames. In this way, a comprehensive overview of all the single structures and their mutual interaction can be obtained. In Figure 5.2 the time step increases with the lines from left to right. The onset of a single structure formation, its temporal evolution with the increasing of its complexity (number of convolution), its interaction with other simple structure to form a new structure (i.e. 2-D vortex couple structure) can be easily highlighted and discussed.

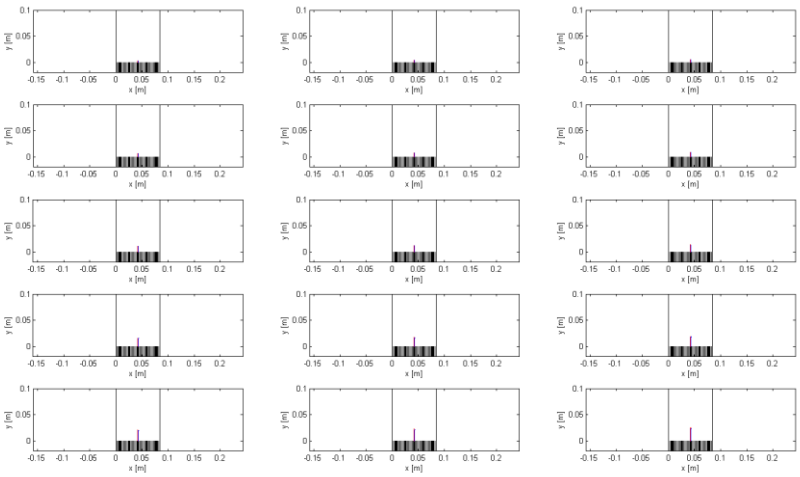
y [m]
x [m]

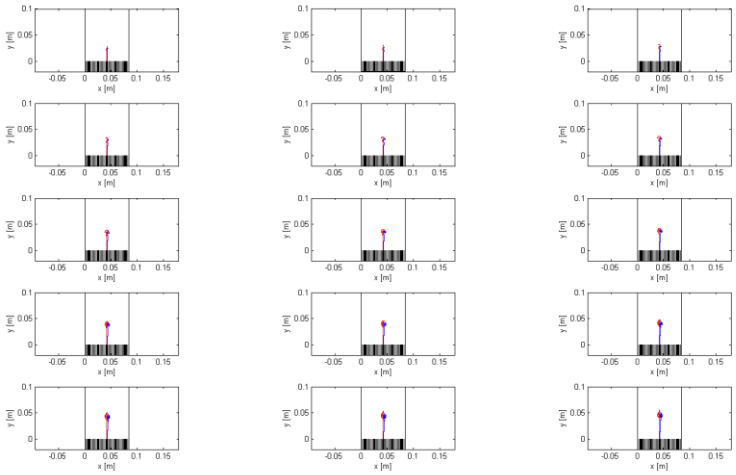
y [m]
x [m]

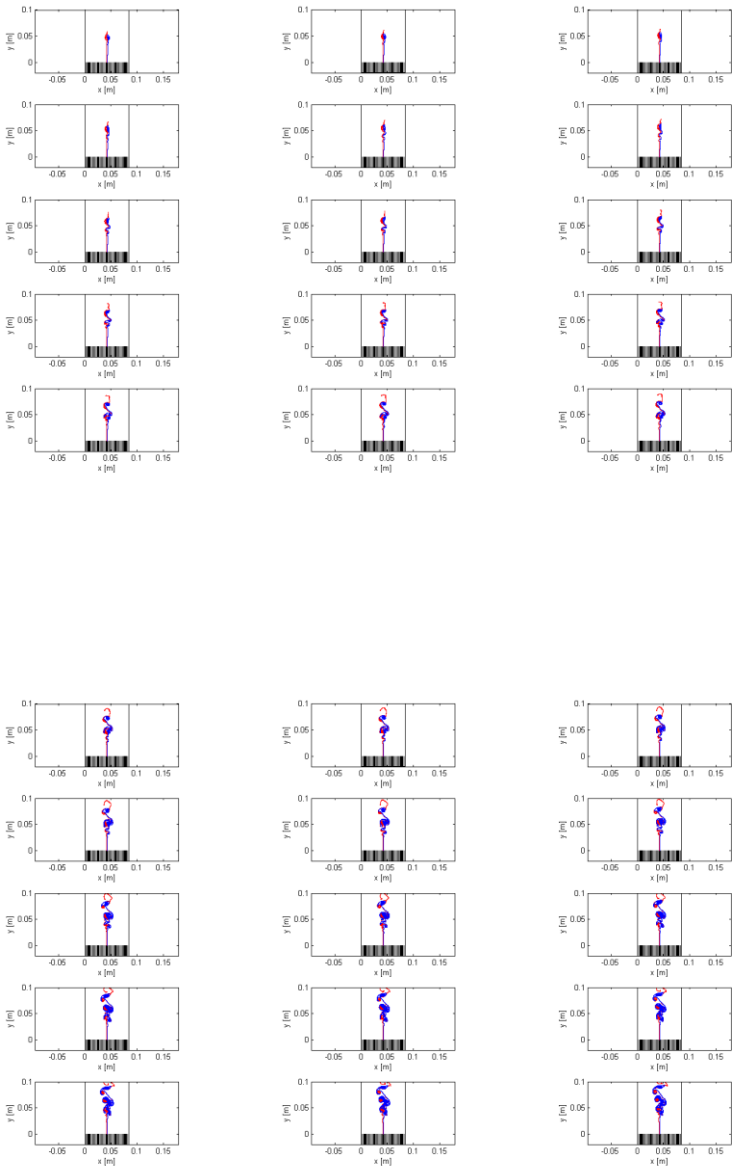

Figure 5.2. Intermaterial surface evolution for several time steps.

Figure 5.3 shows a zoom of intermaterial surfaces evolution reported in Figure 5.2.

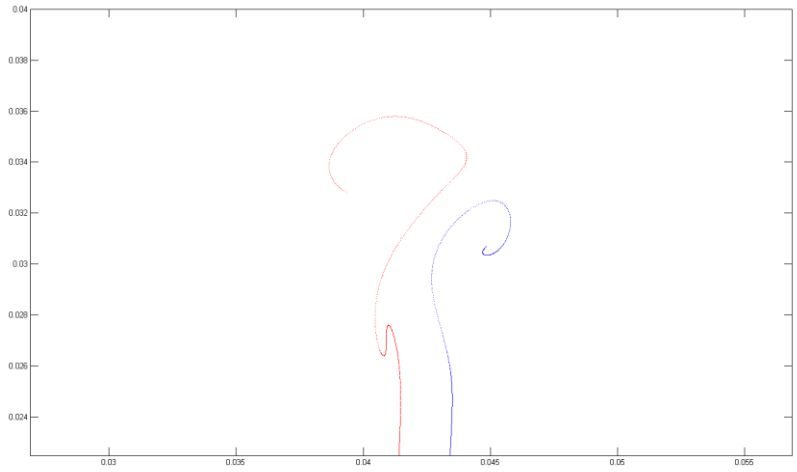

a

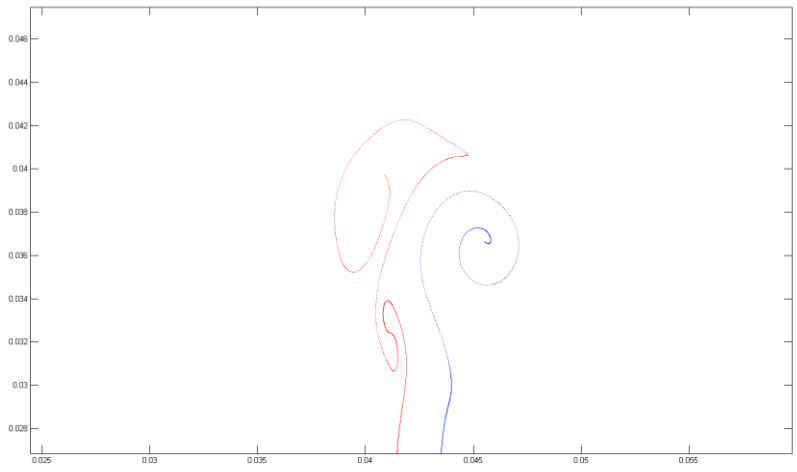

b

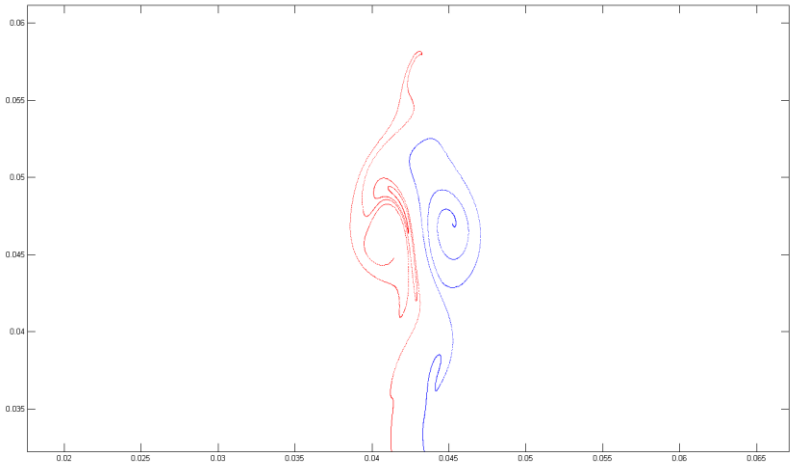
0.06
0.055
0.05
0.045
0.04
0.035
0.02
0.025
0.03
0.035
0.04
0.045
0.05
0.055
0.06
0.065

c

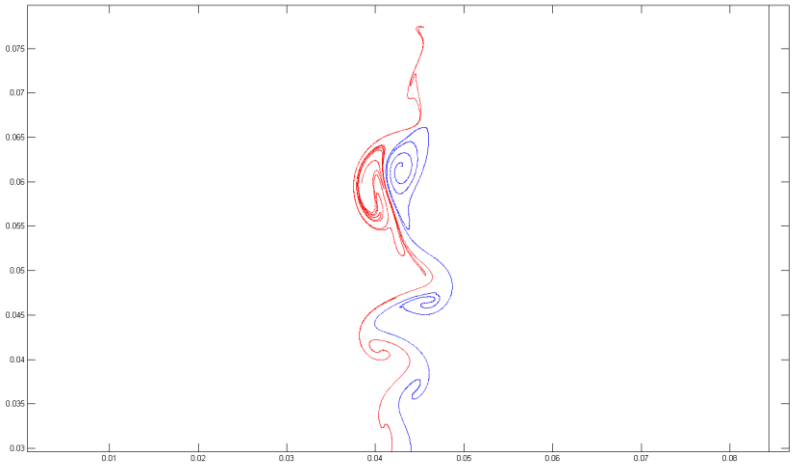
0.075
0.07
0.065
0.06
0.055
0.05
0.045
0.04
0.035
0.03
0.01
0.02
0.03
0.04
0.05
0.06
0.07
0.08

d

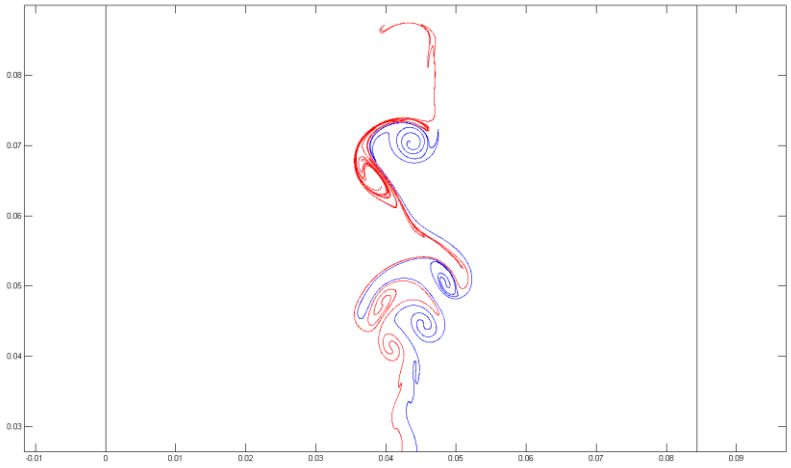
0.08
0.07
0.06
0.05
0.04
0.03
-0.01
0
0.01
0.02
0.03
0.04
0.05
0.06
0.07
0.08
0.09

e

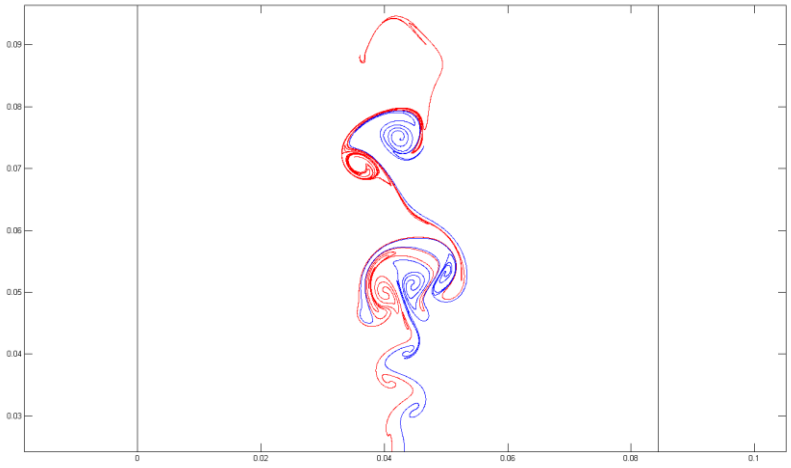
0.09
0.08
0.07
0.06
0.05
0.04
0.03
0
0.02
0.04
0.06
0.08
0.1

f

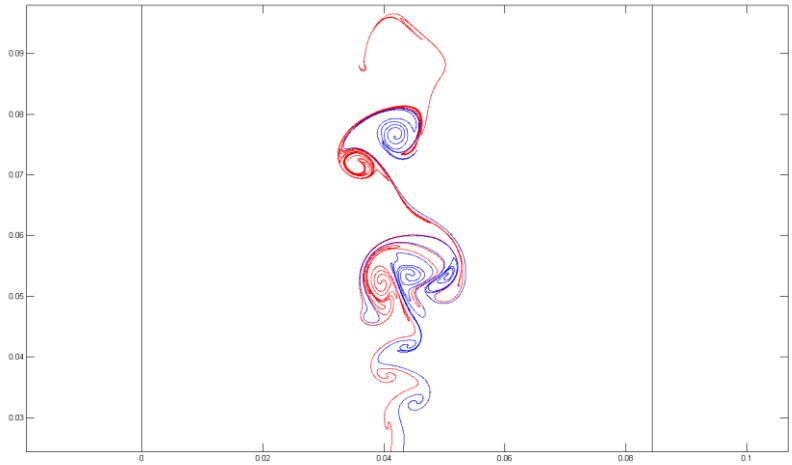

g

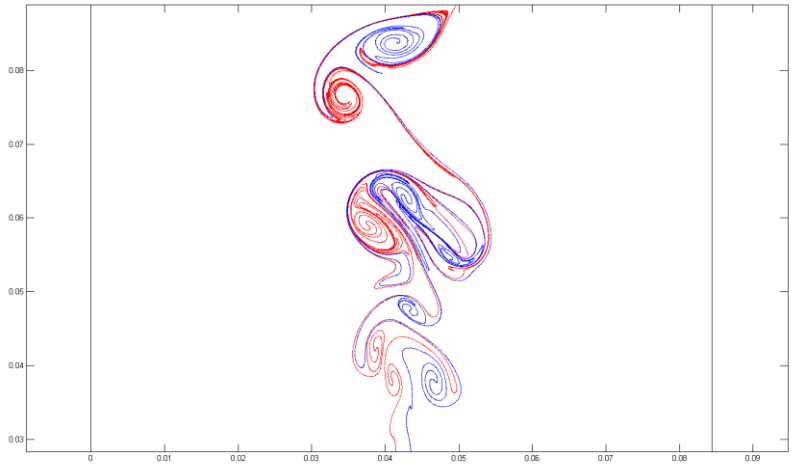

h

Figure 5.3. Details of Lagrangian coherent structures identified during interface evolution at a single time step.

Figure. 5.3a is related to the first time steps. At this time, the onset of two different single structure (a first related to the right interface, a second to the left one) is visible. In Figure. 5.3b such a structures are evolving in two

different convoluted vortex structures, even if they are characterized by a very small number of convolution. Also the onset of a third vortex structure formation (related to the left interface) can be detected. Increasing the residence time (Figure 5.3c), the two single vortex structure can be clearly distinguished. Such a structures are characterized by a number of convolution It is important to note that at this time, the number of convolution of a single structure is increased respect to the structure highlighted in Figure 5.3b, thus, the convolution number is a function of the time. Moreover, for such a frame, the two single vortex structure appear not interacting. Later on (Figure 5.3d), the evolution of the two interfaces reveals that such a structures start to interact, with the formation of a 2-D counter-rotating vortex couples that moves forward toward the outlet section. In more detail, such a new structure is due to a coalescence of different single vortex, reflecting the mutual interaction of single vortex during interface evolution.

The formation of other four single vortex structures are clearly visible at the jet base. The alternate shedding of vortices on the left and on the right side is observable. A comparison between such a structures with that molded previously shows that the complexity of a single vortex structure is strongly related to the residence time. For a fixed time step, structures that formed first are characterized by an higher complexity in terms of number of convolution, stretching factor and dimension (generally, a vortex formed first is bigger that one just formed) compared to those formed after. Furthermore, analysis of Figure 5.3d shows that the first two single vortex structure (interacting) are characterized by braids respect to that detected in Figure5.3c. From a statistical point of view, a braid is an intrinsic topological feature of a vortex structure always formed. However, as highlighted in Figure 5.3d, such a braids are well distinguished only after a mutual interaction of co-rotating vortex structures associated to the same interface. Figures 5.3e and 5.3f show that, increasing the residence time further, the mutual interaction of the two big vortex stop (located at the top of the domain) is no longer visible with the two

single vortex that move away one from each other. At the contrary, the four small vortex at jet base (now more convoluted), start to interact to form a macro-vortex structure. Finally, Figures 5.3g and 5.3h describe the evolution of the macro-vortex structure. In particular, Figure 5.3h reveals that the mutual interaction of the four single vortex structures highlighted previously (Figure 5.3d) involves the formation of a new structure. In particular, it is possible to observe the presence of 2-D counter-rotating vortex couples (located in the middle of the domain) within the macro-vortex structure. Moreover, for such a frames, a large number of vortex structures are present (for the last frame eight different vortex can be detected).

Analysis of the intermaterial surface evolution describing a transitional jet behavior in a 2-D configuration revealed a key feature of the vortex structures previously analyzed. For a such a case (2-D), in fact, the nature of the vortex structure generated can only formed other vortex structure.

Summarizing, all the identified structures (2-D) can be categorize as:

- no vortex structure;
- structure associated with the onset of a vortex structure formation;
- simple vortex structure with small number of convolution;
- simple vortex structure highly convoluted;
- simple vortex structure highly convoluted and with braids;
- 2-D counter-rotating vortex couples structure;
- macro-vortex;
- 2-D counter-rotating vortex couples structure within a macro-vortex structure.

In order to reveal several aspects of Lagrangian coherent structures highlighted previously, Figure 5.2 reports several details of one interface (right) at the highest time step analyzed. In particular, different complex vortex structures

characterized by different convolution number can be detected, together with 2-D counter-rotating vortex couples structure varying nozzle distance. The presence of such a peculiar structure is due to a coalescence of different single vortex, reflecting the mutual interaction of single vortex during interface evolution.

As reported in the introduction, the main purpose of the Ph. D. activities is the re-construction of the mixture fraction Z starting from descriptive parameters associated with the stirring process. Such a parameters are interface-conditioned and can be directly obtained from the interface spatial/temporal evolution. The approach adopted in this thesis follow a logical procedure starting with a quantification of basic quantities, such as particles residence time, to more complex one, ending with the characterization of Z. In this way, this approach is "systematic" in a hierarchical sense (with a pyramid structure), obtaining an evaluation of key descriptive parameters starting from an Eulerian fluid phase simulation and then, implementing a Lagrangian approach for studying the intermaterial surface evolution from which the parameters can be derived; "exhaustive" since the stirring process is descripted in full detail.

5.1.2. Particles Trajectories, Arc length and Velocity Pattern Visualization

Figure 5.4 shows the particles paths for three different particles (randomly chosen) along the calculation domain. Particle denominated with "A" in the picture is injected before particles "B" and "C", as well as "B" refers to a previous time step with respect to particle "C". For a comparison, all the trajectories are reported in a single picture on the right side of Figure 5.4.

First of all, all the trajectories show a similar trend, with particles that move forward toward outlet domain, along a "straight" line. A comparison between different particles paths reveals that only a variation of particle x-position along the path is visible.

It appears evident that a vortex structure, characterizing an intermaterial surface evolution, is represented by a set of several particles that at a fixed time step are located at different positions in the domain. In other words, Figure 5.4 shows that a particle path does not follow the vortex curvature, revealing a key feature of the particle trajectories.

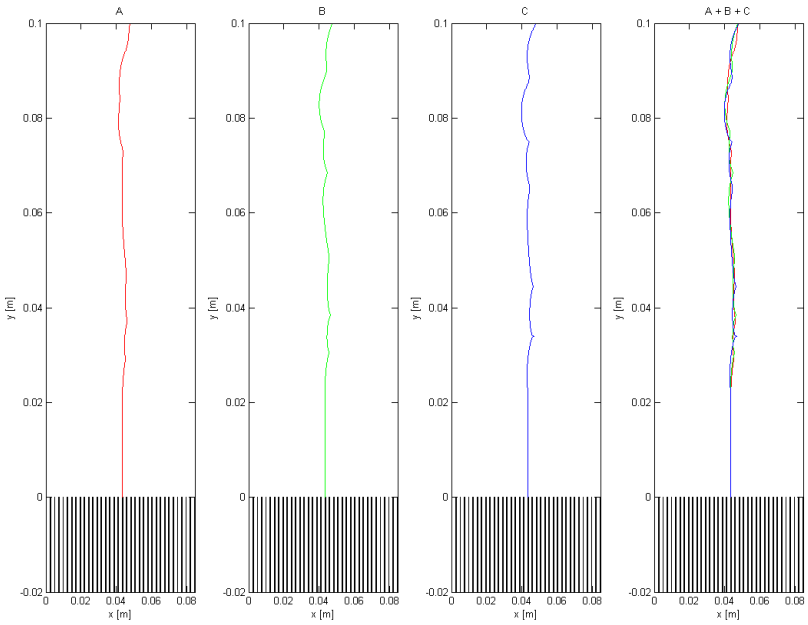

Figure 5.4. Particle Trajectories.

Figure 5.5 shows the temporal evolution of arc length for three different particles (randomly chosen). Also in this case, all the calculated arc length are reported in a single picture on the right side of Figure 5.5.

From a comparison of the reported arc length, it is worthwhile to note that not depending on the particle ID, all the arc length show a similar temporal evolution. In particular, the arc length increases by increasing the residence time. Moreover, since the particles are characterized by different velocity values and position (it is appears clear from particles trajectories analysis), for a fixed particle residence time value, they will be characterized by different values of arc length (path length are different).

Figure 5.6 reports the velocity as function of the polygonal path for three different particles (randomly chosen). Top refers to mean particle velocity, bottom to the instantaneous one.

It is worthwhile to emphasize that not depending on the particle ID, velocity shows a similar trend respect to the polygonal path. In particular, for the first part of the polygonal path the velocity increases for then remain approximately constant by further increasing the arc length value. Moreover, velocity fluctuations are more evident (higher oscillation magnitude), at the first part of the polygonal path.

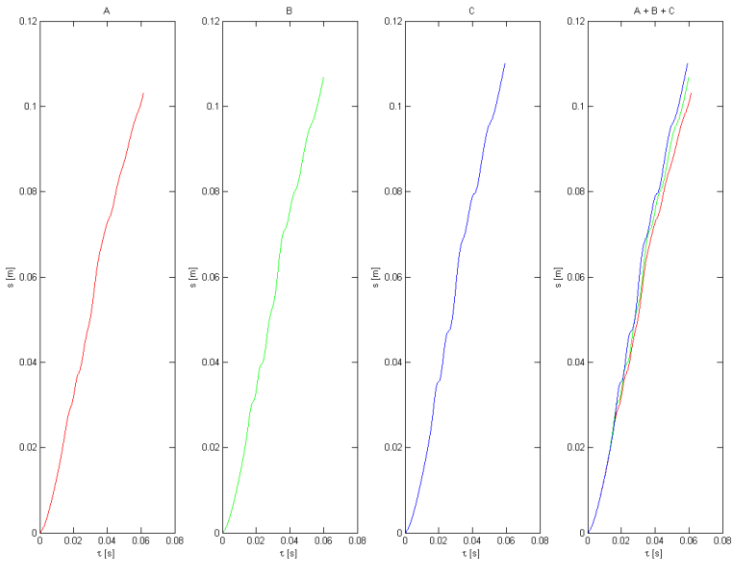

Figure 5.5. Temporal evolution of arc length.

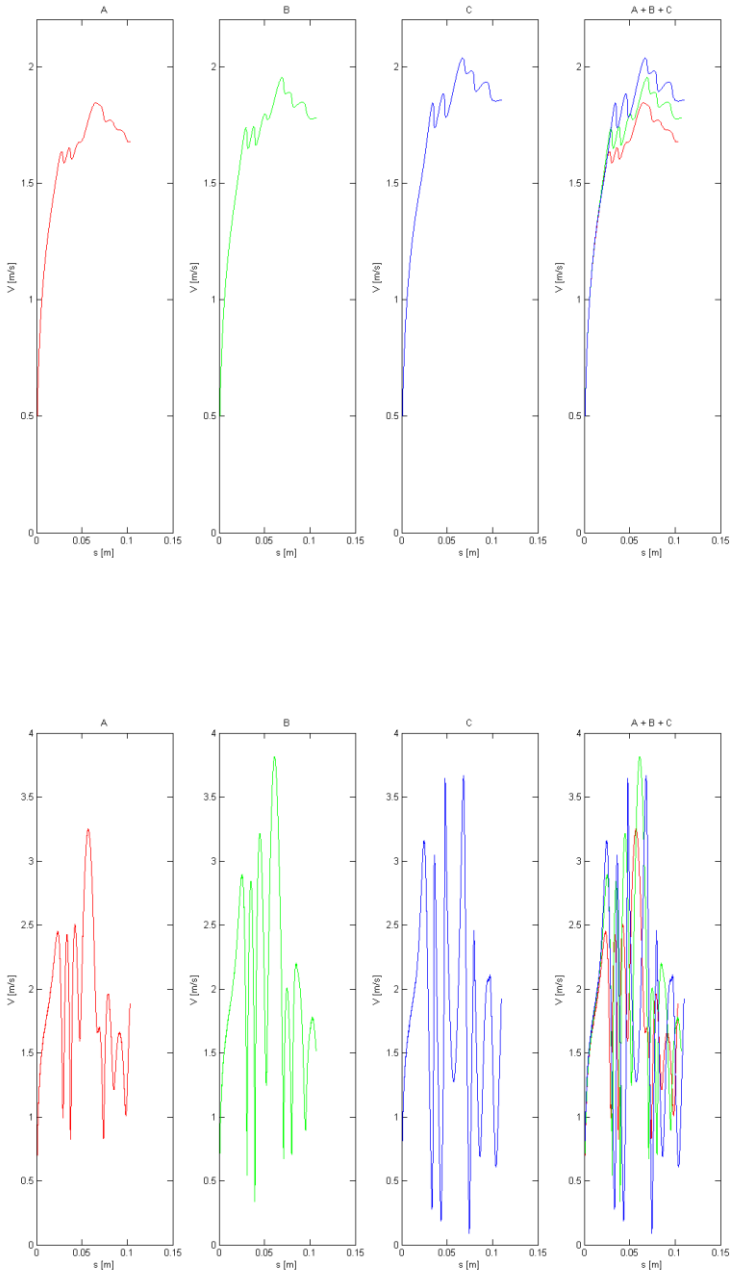

Figure 5.6. Velocity as function of the polygonal path (top) mean velocity; (bottom) instantaneous velocity.

5.1.3. Particles Residence Time

Figure 5.7 shows the map of mean Particles Residence Time (PRT) on the calculation domain. Such a parameter has been evaluated determining the arc lenght of the polygonal path of a single particle using the Pitagorean theorem and dividing it at each time step by the mean velocity of the fluid phase flow. As it possible to highlight from the map, generally, the PRT increases (approximately linearly) by increasing the nozzle distance, reaching a maximum value at the end of the domain. However, long mean residence time have been detected also at the middle of the configuration (right side of jet). Such a zone is characterized by a strong vorticity, so that a particle that is found in this zone remains more time before leaving it. In this regard, the mean PRT could be a first evaluator for vortex structure identification/characterization.

Figure 5.8 reports the pdf of mean Particles Residence Time at different monitoring point. In particular, the graphs shown are representative of the twenty-five cells located at the middle of the map reported in Figure 5.4. The abscissa is the overall residence time scale.

PDF reveals other aspects of PRT. More specifically, several types of pdf can be detected depending on region investigated: uni-modal and bi-modal and multi-modal. Uni-modal case is representative of that zones where the interfaces interaction is not strong and the vortex structure are characterized by a small number of convolution. At the contrary, bi-modal and multi-modal pdf of PRT reveals a region characterized by a strong mutual interaction between interfaces and higher level of vorticity. The presence of multi-modal pdf can be directly related to an high number of convolution Furthermore, such a pdf is connected with longer particle residence time respect to the other pdf analyzed.

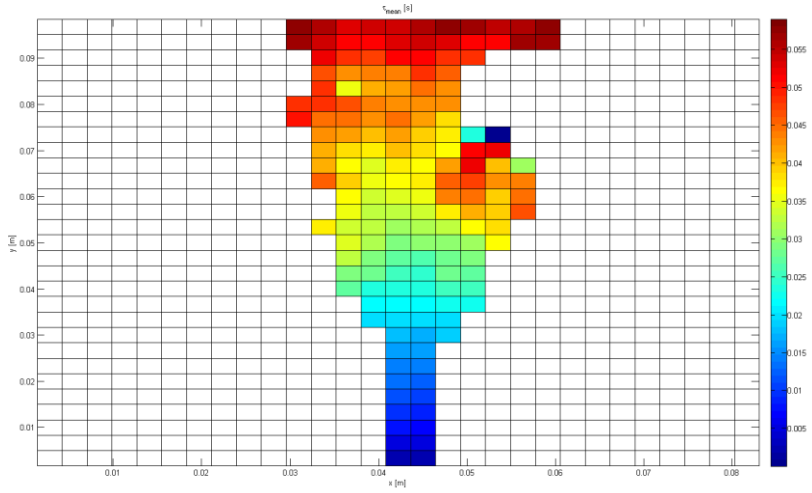

Figure 5.7. Map of the mean PRT.

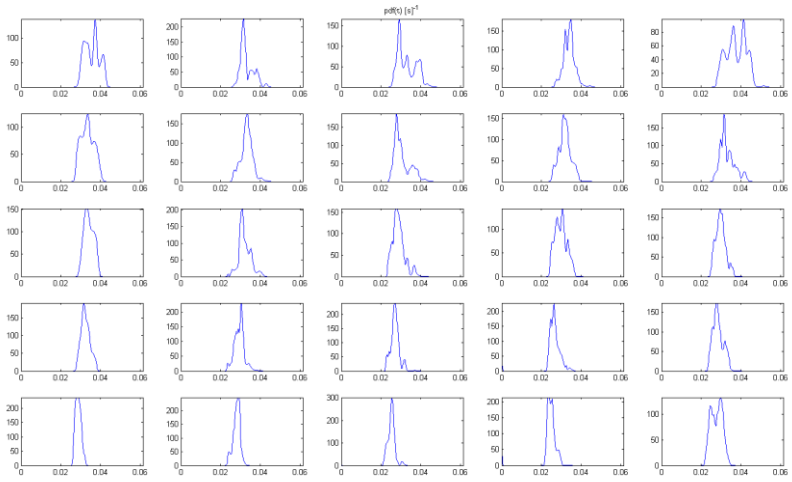

Figure 5.8. PDF of mean PRT at different monitoring point.

Figure 5.9 reports the temporal evolution of the arc length (s), stretch ratio (SR) and stretch rate (K_{SR}) calculated for three successive particles. Such a parameters are descripted in Chapter 2.

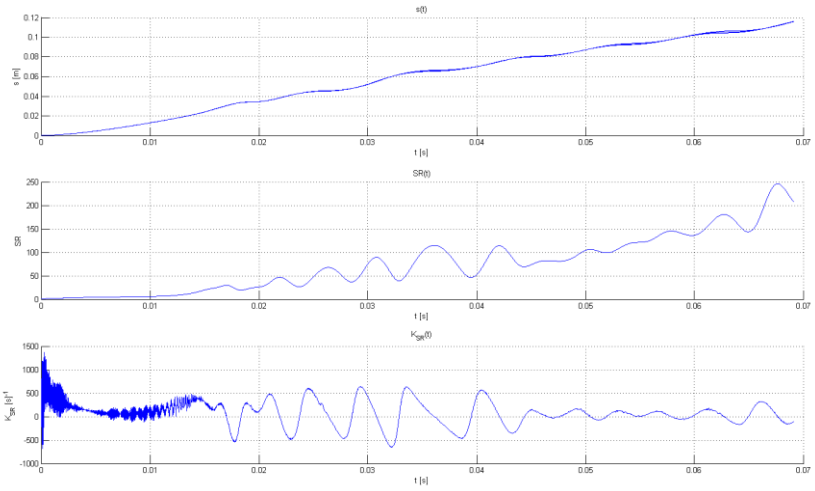

Figure 5.9. Arch length, stretch ratio and stretch rate as function of residence time for three particles.

The arc length (s) shows a similar trend for all the three particles considered, excepted for some residence time values for which the arc lenght results different. More specifically, analysis of arc lenght evolution indicates that these points are characterized by an extension/contraction of the intermaterial surface. Stretch ratio (SR) increases approximately linearly with the residence time. Maximum/minimum of the curve are representative of the interface extension/contraction events, respectively.

Moreover, it is possible to note that SR does not increase monotonically, as it could expected; instead, a comparison between SR and K_{SR} trend revealed that the element of intermaterial surface is subjected also to a contraction.

5.1.4. Stretch Ratio and Stretch Rate

This section reports analysis of stretch ratio (SR) and stretch rate (K_{SR}). As reported in Chapter 2 such a quantities are of interest since they help in characterize the evolution of an intermaterial surface.

Consider, for example, a 2-D surface at time t_0 as it is sketched through its linear section. Every point of the surface follows a definite trajectory. At time t all these points together will make up a new surface which besides being translated and rotated is also extended or contracted. In the aforementioned figure material surfaces are sketched starting from a surface arbitrarily fixed at the point t_0. In theory a material surface cannot became discontinuous even if in practice its detection can be subject to the limits already discussed in conjunction with the interface. Surface stretching is defined as the temporary evolution of the surface area. The stretch ratio, or SR, is the ratio between the material surface area at time t and the area at time t_0, for which $\mathrm{SR} = \delta A(t)/\delta A(t_0)$.

The stretch rate K_{SR} is the relative change of the stretch ratio, SR, for which $K_{SR} = D(\ln SR)/Dt$.

Figure 5.10 reports the temporal evolution of stretch ratio (SR) for three particles (randomly chosen).

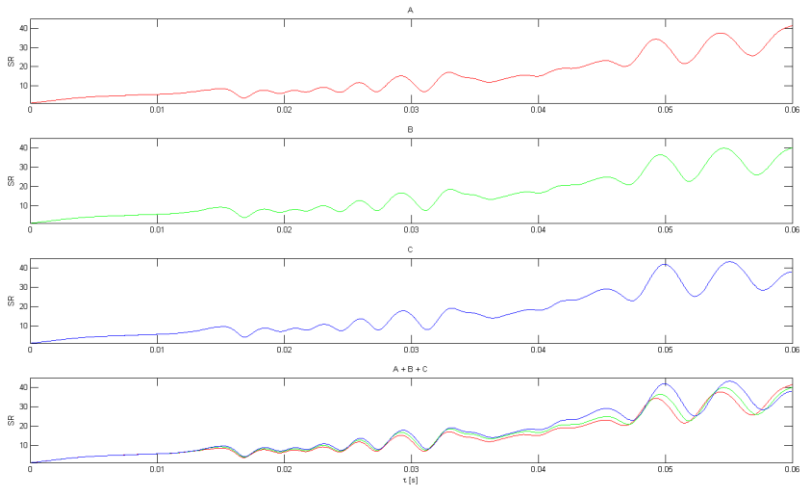

Figure 5.10. Stretch ratio as function of residence time for three particles.

It is worthwhile to note that SR increases almost linearly with time, so that its trend could be described by adopting a straight line fit. The maximum value detected for SR is about 40. For completeness, the map of mean SR and its PDF are reported (Figures 5.11 and 5.12). A good agreement with experimental data obtained by [9] is found. Also, similar PDF have been obtained.

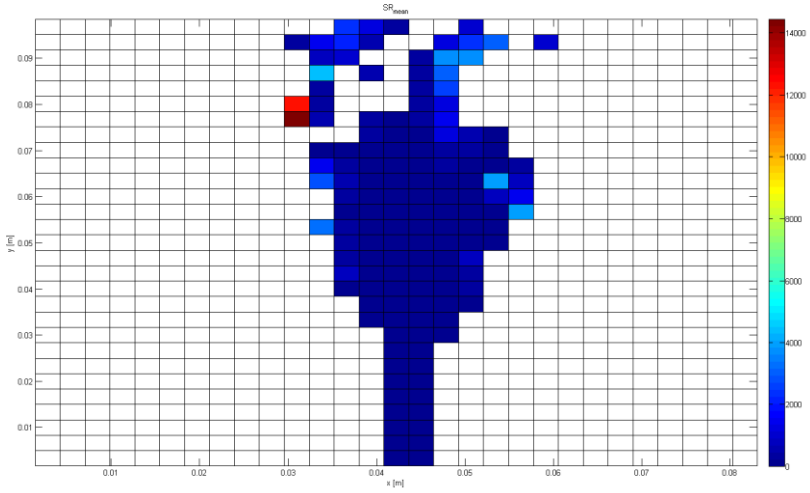

Figure 5.11. Map of the mean SR.

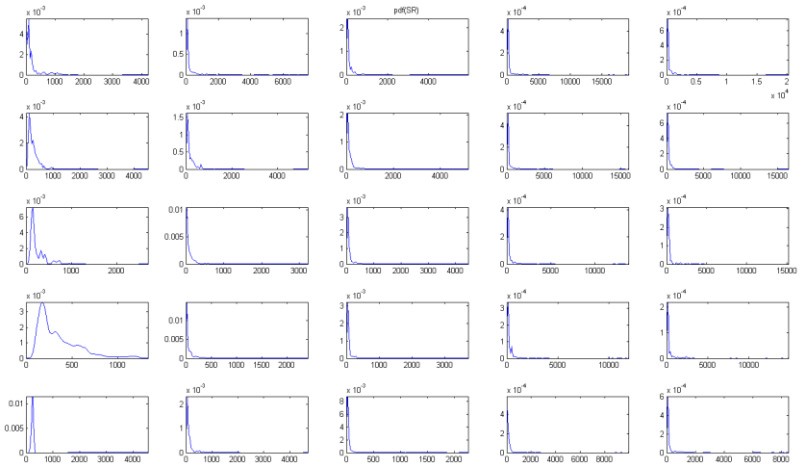

Figure 5.12. PDF of SR at different monitoring point.

Figures 5.13 reports the temporal evolution of stretch rate for three particles (randomly chosen).

It is worthwhile to note that SR remains almost constant with time. Such a trend suggests that the deformation of the intermaterial surface for the system under investigation is not a function of the time (deformation is not dependent of time).

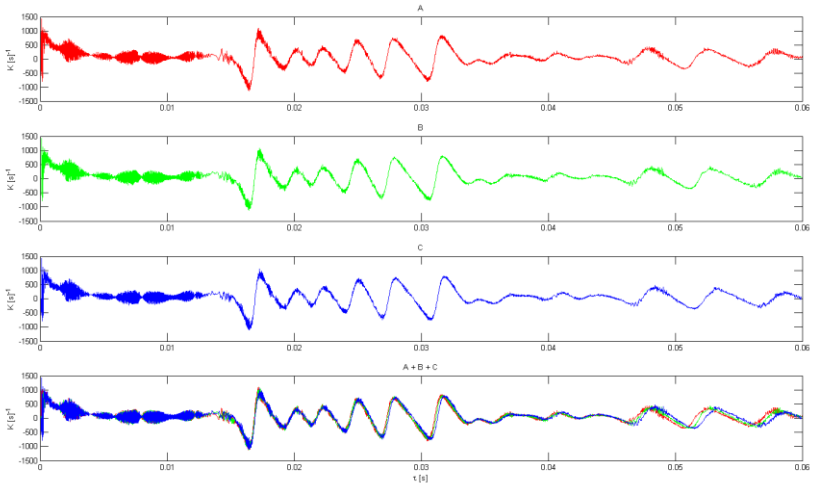

Figure 5.13. Stretch rate as function of residence time for three particles.

For completeness, the map of mean K_{SR} and its PDF are also reported (Figures 5.14 and 5.15).

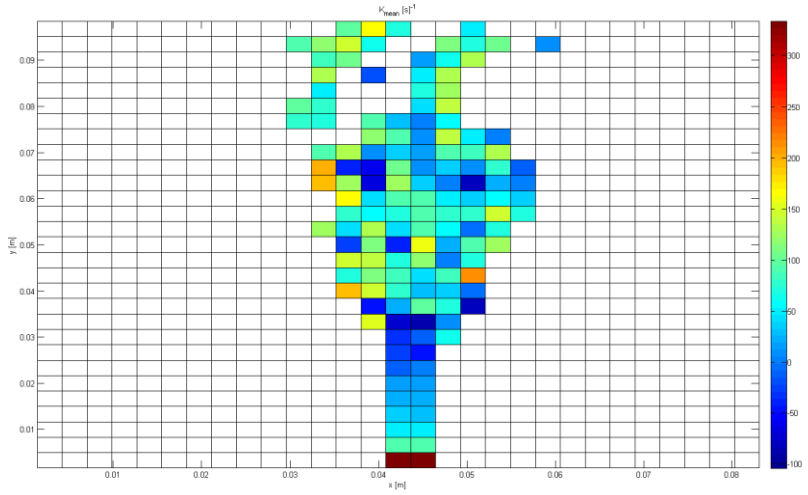

Figure 5.14. Map of the mean K_{SR}.

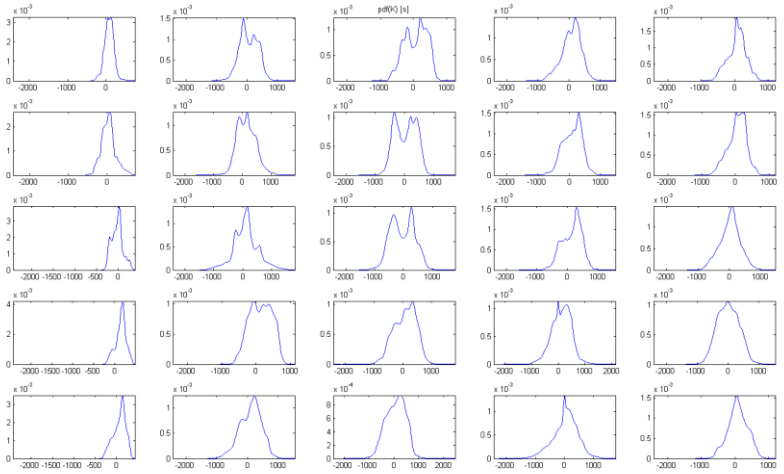

Figure 5.15. PDF of mean K_{SR} at different monitoring point.

Figures 5.16 and 5.17 report the map of the mean stretching (or squeezing) factor $\gamma = \sqrt{\overline{SR^2}}/SR$ on the calculation domain. As it possible to highlight from the map, the region characterized by an higher vorticity, the value of the

stretching factor is maximum and close to 1; in other words such a region is associated with a approximately constant stretch rate, with a balance between extensions and contraction of the intermaterial surface.

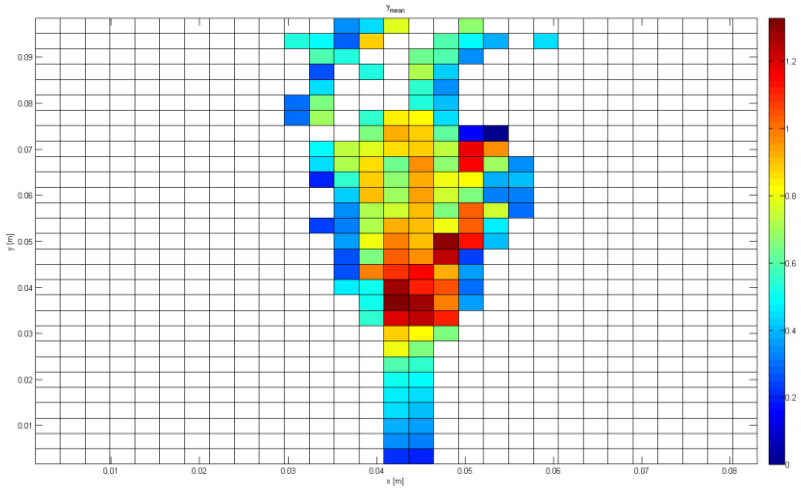

Figure 5.16. Map of the mean stretching (or squeezing) factor.

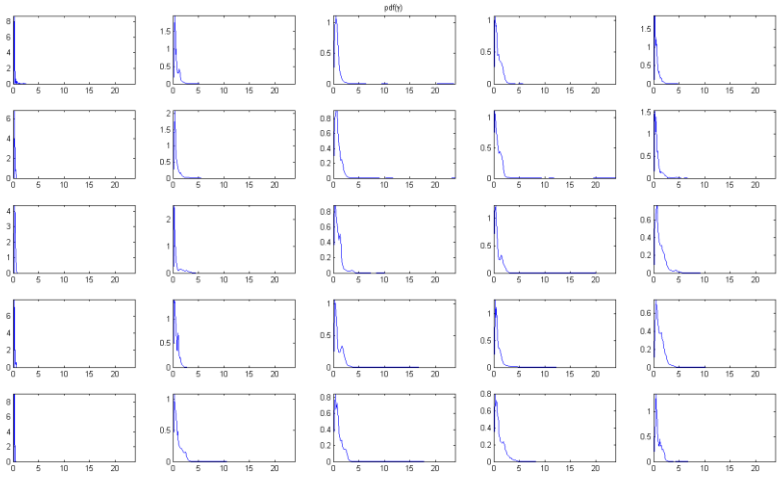

Figure 5.17. PDF of the mean stretching (or squeezing) factor.

Following the logical procedure descripted previously, it is important to remind that a 1-D unsteady diffusive layer is described by the equation:

$$\frac{\partial Z}{\partial t} - \mathcal{D}\nabla^2 Z = 0 \qquad (5\text{-}1)$$

This is the conservation equation of the mixture fraction Z in non-reactive conditions and for constant density. If the initial condition (at $t = t_0$) is a step function the evolution of Z can be obtained from the conventional integration of Z. The integration exploits the so-called Boltzmann variable $\xi = x/\sqrt{4\mathcal{D}t}$ a combination of x and t. Adopting the right boundary equation, a solution for Z can be obtained [3]. An approximate expression of the thickness of the incompressible diffusive isothermal layer δ_m^{ns} is given by the value of x corresponding to $Z = 0.08$ or $Z = 0.92$. This is given by $\delta_{0.92} = \sqrt{4\mathcal{D}t}$ which is exactly the quantity by which the x variable is scaled to give the Boltzmann variable. Therefore, $\xi = x/\sqrt{4\mathcal{D}t} = x/\delta_m^{ns}$ is equal to 0 at the center of the diffusive layer and is equal to 1 in the marginal areas where Z assumes the values of $Z = 0.08$ or $Z = 0.92$. δ_m^{ns} is defined as the thickness of the diffusive layer. It grows in as $\sqrt{4\mathcal{D}t}$ or it moves at speed $w = \sqrt{4\mathcal{D}}/2 \cdot 1/\sqrt{t} = \sqrt{\mathcal{D}/t}$.

For a stretched case, the thickness of the diffusive layer is formally the same obtained in the unsteady non-stretched case but, in this latter case, the diffusive layer thickness δ_m differs from the un-stretched one, δ_m^{ns}, for a stretching (or squeezing) factor γ. In principle SR and the stretching factor can be either greater or smaller than 1 but in general SR is greater than 1 and the stretching factor is lower than 1. This is the condition that controls the possibility of a true mixing of the flows. In fact, the thickness of the diffusive layer increases because of the diffusive effects, as it occurs in the un-stretched

case whereas the iso-surface stretching around the intermaterial line reduces the mixing layer thickness. The same occurs to any structure that evolves in the mixing layer. For instance, a diffusion flame with a finite thickness, in which an oxidation reaction takes place, will be stretched in the same way of the intermaterial surface.

Figures 5.18 and 5.19 report the map of the mean δ_m (stretched case) on the calculation domain and the PDF of δ_m, respectively. Analysis of the map reveals that the highest value of δ_m are present at the right interface, instead the smallest values at the left one, suggesting that a more intense vortex structure is present in the right region. Moreover, pdf analysis highlighted that such a parameter is strongly affected by interface evolution. The PDF associated with the left part of the monitoring region are characterized by a Dirac-like behavior, suggesting that at such a zone is associated a well/defined value of the diffusive layer thickness (revealing an absence of a strong vortex structure in this zone).

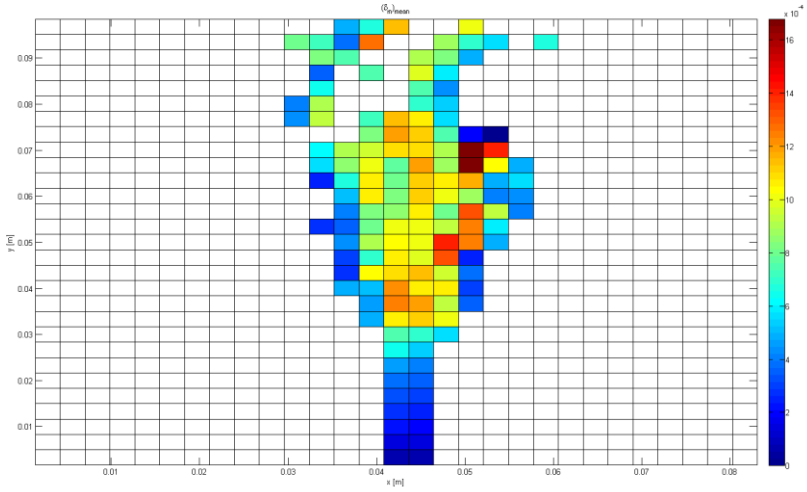

Figure 5.18. Map of the diffusive layer thickness.

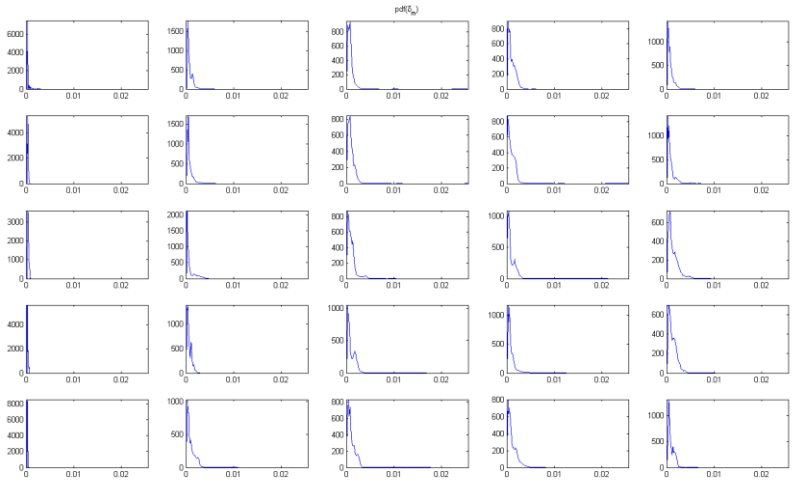

Figure 5.19. PDF of the diffusive layer thickness.

Instead, bi-modal PDF of δ_m have been detected for the right part of the monitoring region, reinforcing the fact that such a zone is vortex-dominated. In fact, since δ_m increases linearly with the residence time, it is plausible that an high-vorticity region is characterized by a non-uniform distribution of the mixing layer dimension.

5.2. Unsteady autoigniting layerlet

In the previous sub-sections, they were shown two important aspects related to some limitations of the flamelet approach for turbulent non-premixed flows:

- it is not capable of modeling unsteady effects of ignition;

- flame thickness should be sufficiently small compared to the turbulent length scales.

Hence if chemistry is slow, i.e. the reaction layer is not thin (for example in MILD combustion processes), or unsteady effects are relevant, the flamelet assumption is not valid.

To overcome these limitations, a different approach, named "layerlet", is here adopted [12].

A layerlet is an unsteady diffusive layer characterized by a finite value of its thickness δ_m (that tends to zero if a layer degenerates into an infinitely thin layer).

Unsteady combustion regimes are of interest for many combustion processes because they describe part of the stabilization process. A system with internal recirculation is one of the possible examples of unsteady combustion process. In fact, heated fuel injected in an exhausted flue gas stream with residual oxygen present yields Hot Fuel Diluted Oxidant (HFDO) conditions. Eventually, air mixed with an inert high-temperature flow (such as from a recirculated flow) yields Hot Oxidant Diluted Oxidant (HODO), which can be mixed with fuel at room temperature. Of course, among these exemplificative asymptotic conditions, all intermediate and mixed conditions can be created with partial preheating and dilution of both streams.

Some of these configurations, specifically HODF and HFDF, have been addressed in this section in unsteady conditions [12], because they can be compared directly with the steady results previously presented.

The analysis has been performed following the same approach. It consists of detailed simulations of the thermo-chemical patterns in a dense grid of input parameters synthesized in regime diagrams, and it differs from the other approaches only in the inlet conditions. Therefore, the results are highly comparable with each other, and the discussion on their implication extends the previously outlined conceptual framework.

The study of an unsteady one-dimensional diffusive layer was performed by means of the opposed jets configuration. The attention has been focused on the

system in which an undiluted air stream is always fed in counter-flow toward a nitrogen-diluted methane jet with a different fuel molar fraction X_f. Three types of preheating conditions were established:

- Preheating of the air (room temperature for the fuel), referred to as a hot oxidant diluted fuel (HODF) condition.

- Preheating of fuel (room temperature for the air), referred to as a hot fuel diluted fuel (HFDF) condition.

- Preheating of both streams with the same temperature, referred to as a isothermal (ISO-T) condition.

A structured 2-D mesh, generated with Gambit, was used. It consists of 4×1000 quadrilateral cells with a uniform spacing of $10^{-5}\, m$. Velocity inlet boundary conditions have been used to define the flow velocity at the fuel and oxidant inlets, while outflow boundary conditions were used to model flow exits. Numerical analysis has been performed with FLUENT by using, as ChemKin-import mechanism, the GRI 3.0 mechanism implemented without the NO_x reactions [33]. The flow regime is laminar, so there is no need to introduce a turbulence model.

Simulations have been performed at atmospheric pressure for a CH_4/N_2 jet with a fuel molar fraction of $1, 0.5, 0.3, 0.15$ and 0.07, $T_o = 300\, K$, and T_{in} which ranges from 1000 to $2200\, K$. The initial distribution of the mixture fraction, velocity, temperature and species mass fractions has been set equal to a step function from the inlet values.

The structure of the reactive zone has been analyzed by an evaluation of temperature (T) profiles as a function of the mixture fraction (Z) along the

axial coordinate of the system evaluated on the nitrogen mass fraction, which is conserved in the kinetic scheme used in this case.

The ensemble of the temperature/mixture fraction profiles for each preheating and dilution condition allow three relevant characteristic times, partially used previously by other authors [34], reported in Figure 5.20:

- the minimum ignition time (τ_{IGN});
- the temperature-maximization time (τ_{MAX});
- the stabilization time (τ_{STAB}).

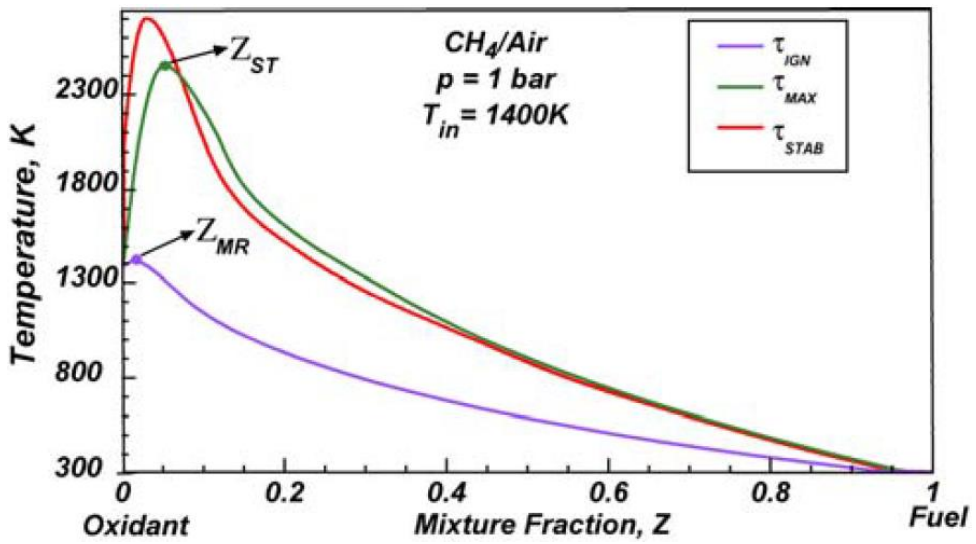

Figure 5.20. Characteristic times for $p = 1\ bar$ and $T_{in} = 1400\ K$.

The minimum ignition time (τ_{IGN}) reported in this thesis is the time at which the system reaches a threshold of $10\ °C$ above the temperature of the frozen

state for the first time, due to heat release. This minimum occurs at a mixture fraction defined as the most reactive one (Z_{MR}).

The temperature-maximization time (τ_{MAX}) is defined as the time at which the peak temperature in the $T-Z$ plot is localized at the stoichiometric mixture fraction value. Its computation is straightforwardly obtained by the temporal evolution of temperature at a fixed mixture fraction.

Lastly, the stabilization time (τ_{STAB}) is defined as the time at which the system reaches its steady-state temporal profiles. It is evaluated by searching the maxima of the temperature differences between the current values and the corresponding steady-state solutions at fixed times.

The overall behavior of the unsteady MILD combustion process is shown in Figure 5.21. The figure consists of nine plots, which refer to nine selected feeding conditions: three for each type of preheating condition at different fuel dilution levels. More specifically, the first three plots in the first left column refer to the HODF condition with an air temperature of $T_{in} = 1400\,K$; the three central ones refer to isothermal (ISO-T) conditions in which the fuel jet and the oxidant jet are fed at the same initial temperature ($1400\,K$); and the three plots on the right column refer to the HFDF with an inlet temperature of the diluted fuel of $2200\,K$. The choice of such a high temperature is related to the use of the results for exemplificative purposes. In fact, at lower temperatures, the HFDF condition does not always present ignition for different dilution levels. The plots aligned on a single row have the same dilution level. The first one is the undiluted case at $X_f = 1$, the second row is an intermediate dilution case with $X_f = 0.5$, and the third row reports very diluted cases (classified as MILD conditions) at $X_f = 0.07$.

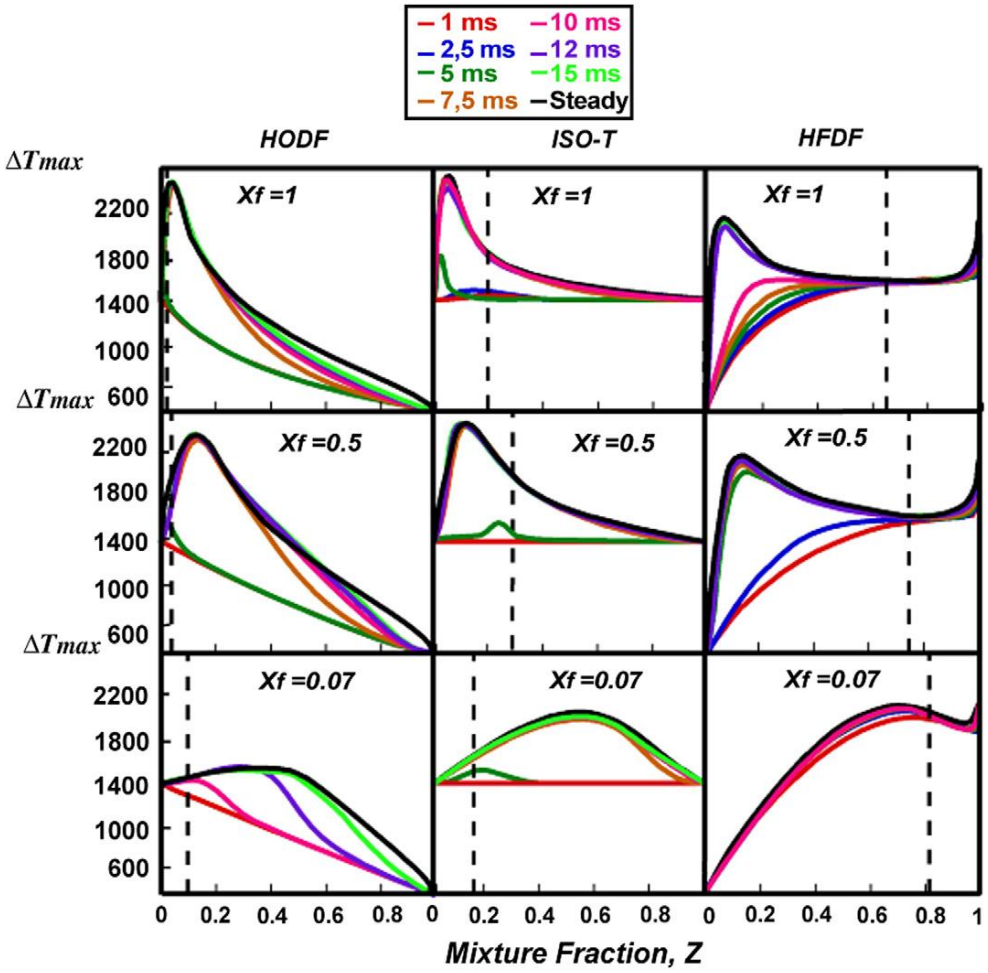

Figure 5.22. Temperature profiles with respect to time, which refers to nine selected feeding conditions at different fuel dilution levels ($X_f = 1, X_f = 0.5, X_f = 0.07$).

Temperature versus mixture fraction profiles are reported; in each individual plot, the profiles are parameterized for eight values of the time delay (with respect to the initial condition) uniformly distributed between $1\,ms$ and $15\,ms$ and are color-coded, as shown in the inset. The steady-state profile is also reported with pale black line.

The first plot in the left top corner shows the ensemble of the temperature profiles divided into two main sub-sets of profiles. The first ensemble of profiles before the ignition is fused into a nearly rectilinear line, which approximates

the frozen mixing line. The first (and only) colored profile that clearly detaches from the asymptotic lines pertains to the temperature profile evaluated at $5\,ms$ after the initial time. This profile can be considered representative of the autoignition process, even though the temperature increase is much higher than that used in the definition ($10\,°C$), which cannot be appreciated in this representation because of the choice of temperature scale. The profile reported in the figure for $7.5\,ms$ cannot be distinguished from the others and from the steady-condition profiles when Z is less than 0.2. It is fused with the other profiles of the mixture fractions less than 0.2, i.e., the temperature profiles show a "jump" when passing from autoignition conditions to the stabilized combustion conditions in a temporal range between 5 and $7.5\,ms$.

As matter of fact, a slow shift from the temperature profile at $7.5\,ms$ to the temperature profile at $15\,ms$ can be appreciated in the mixture fraction range greater than 0.2. In particular, at $Z = 0.5$, the maximum increase of $300\,K$ is shown in the figure, and three profiles are distinguishable from each other.

In the second row of HODF cases, the methane is diluted with nitrogen at a molar fraction of $X_f = 0.5$. The general behavior of the temperature profile is quite similar to those reported for $X_f = 1$, as previously described. The main difference is the shift in the maximum at $Z = 0.15$, which is consistent with the shifts observed for stoichiometric mixture fractions, which also shift from 0.05 in the undiluted case to 0.15 for the diluted one. Furthermore, the bottom line, which represents the frozen mixing condition, is significantly different. It is positively curved at $X_f = 1$ and is nearly straight at $X_f = 0.5$.

This behavior is due to the influence of the specific heat capacity, which, for methane, is more than double that of air. The frozen mixing line is straighter for more diluted fuels. In fact, the dilution with nitrogen makes the

specific heat capacities similar, and the mixing rule is no longer valid for such mixtures.

Lastly, the ignition time for this partially diluted case is $5\,ms$. Additionally, in this case, the isolated curve reported with a green color is distinguishable from the other curves whose frozen and steady-state curves are fused.

The similar behavior described for these two plots is not confirmed under the highly diluted condition at $X_f = 0.07$, which is representative of a MILD combustion process, reported in the third row of the HODF column. In this case, the temperature profiles show a gradual increase in the maximum temperature with increasing time, starting from the first profile at $10\,ms$, which can be considered representative of the autoignition process. The times for the temperature profiles reported in the figure were purposely chosen to make the curves distinguishable from each other and uniformly spaced. This stresses the slowness of autoignition process, particularly when the profile distribution is compared with those in other plots. This comparison is possible by virtue of the use of the same times for which the temperature curves have been reported for all the plots, i.e., the fusion of the temperature profiles on one of the two limit conditions (frozen and steady-state) is itself informative when the two times between which the "jump" occurs are identified. This fusion of the profiles is the case for the three plots reported in the central column (ISO-T), which refers to the three cases in which the fuel jet and the oxidant jet are fed at the same initial temperature ($1400\,K$) so that the frozen mixing line is horizontal and straight. The first two plots, at $X_f = 1$ and $X_f = 0.5$, are similar to the corresponding plots on their left in HODF. The temperature profiles show a "jump" within the same time range. In contrast, for ISO-T conditions, the profile distribution is significantly different under the diluted condition at $X_f = 0.07$. The "jump" is observed only under the ISO-T conditions, reported in the central lowest plot, whereas the aforementioned

"slow graduality" is observed under HODF conditions. A different behavior is shown for the hot fuel diluted fuel (HFDF) conditions, as reported in the third column on the right in the figure. The most diluted conditions in the lowest row show that the early reactivity is due to the pyrolysis process.

In fact after $1\,ms$, all the temperature profiles show values lower than those shown in the frozen profile on the right of $Z = 0.8$. Then, a positive temperature increase is shown in the temperature profile at $2.5\,ms$ for the mixture fraction range centered around $Z = 0.6$. For the less-diluted conditions at $X_f = 0.5$ and $X_f = 1$ (in the center and in the top of the column, respectively), the pyrolysis region (identified by the zone with temperature less than the frozen one) develops over a wider range, and the first oxidation activity is shifted toward the stoichiometric values. The plots of the combustion regimes, in terms of the maximum allowable temperature increase (ΔT_{max}) and inlet temperature of the preheated reactant (T_{in}), are reported in Figures 5.22 and 5.23 such that they are outlined for both the HODF and HFDF regimes under the steady-state conditions reported previously in this section. The pink, red and blue regions represent the feedback regime, the high-temperature combustion processes and the MILD combustion processes, respectively. It is worthwhile to note that in MILD combustion the process cannot be sustained without preheating the reactants. The black dashed areas are the transitional regions where the existence of multiple steady states has been identified with ΔT_{max} values greater or less than $\Delta T_{max}/MILD$, as also reported in Figures 5.22 and 5.23. Isolines at the fixed autoignition time, the maximization time and the stabilization time have been drawn on these plots with solid, dashed and dashed/dotted lines, respectively.

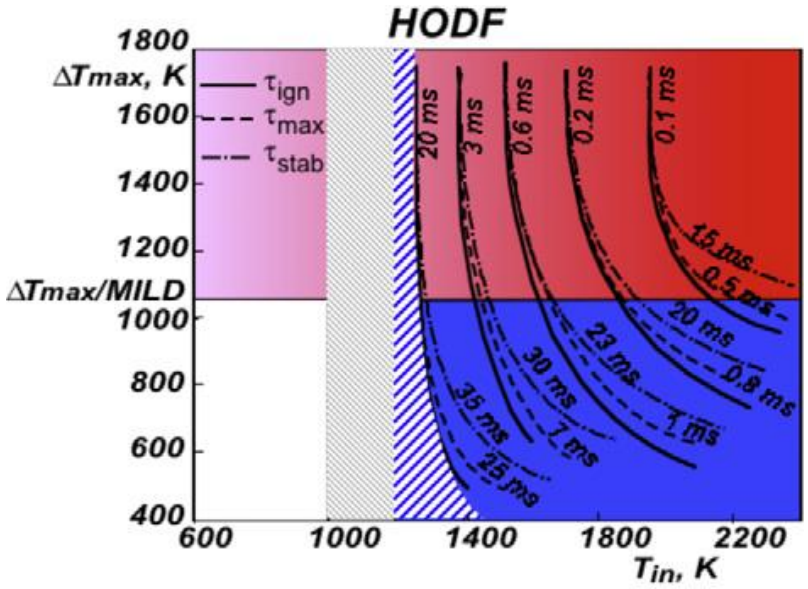

Figure 5.22. Map of the behaviors under HODF conditions for $p = 1\ bar$ and $K_0 = 100\ s^{-1}$. Iso-lines at the fixed autoignition time, the maximization time and the stabilization time have been drawn with solid, dashed and dashed/dotted lines, respectively.

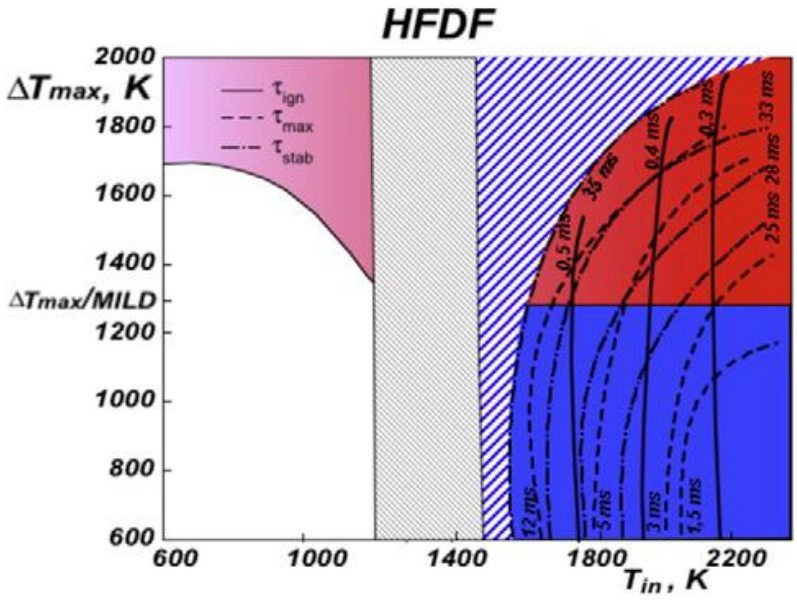

Figure 5.23. Map of the behaviors under HFDF conditions for $p = 1\ bar$ and $K_0 = 100\ s^{-1}$. Iso-lines at the fixed autoignition time, the maximization time and the stabilization time have been drawn with solid, dashed and dashed/dotted lines, respectively.

The autoignition-time iso-lines for the HODF case, shown in Figure 5.22, exhibit nearly hyperbolic behavior with an easily identifiable vertical asymptote. These iso-lines also exhibit a tendency to become more horizontal for inlet-temperature values.

This tendency, in turn, indicates that τ_{IGN} depends only on T_{in} in the high-temperature combustion (red-colored) region, whereas it tends to depend on ΔT_{max} and T_{in} in the MILD combustion (blue-colored) region. The value of τ_{IGN} is less than one millisecond for T_{in} values greater than $1600\,K$; it then increases exponentially and attains $\tau_{IGN} = 20\,ms$ for $T_{in} = 1300\,K$, passing through $\tau_{IGN} = 3\,ms$ for $T_{in} = 1400\,K$.

It is interesting to note that for inlet temperature lower than those on the left of the autoignition iso-lines at $20\,ms$, no ignition occurs. This region is shown in Figure 5.22 with a dashed blue color, which extends the black-dashed transitional area into the high-temperature combustion and MILD regions.

The maximization times τ_{MAX}, i.e., the time required to develop the reactive mixing layer in correspondence of the stoichiometric mixture fraction, exhibit similar trends and range within the same order of magnitude as the autoignition times.

In contrast, for the stabilization time τ_{STAB}, even though their iso-lines have similar trends as those of the other two time values, their values are significantly higher and always range within the same interval between 15 and $35\,ms$.

The behavior of the characteristic times for HFDF is different with respect to those of HODF. In fact, for HFDF, all of the times are approximately perpendicular to the abscissa in the MILD combustion region, which shows that all of them can be considered to depend only on the inlet temperature T_{in}. In contrast, two of the characteristic times, specifically the maximization and

stabilization times, bend in the high-temperature combustion region (red-colored region) in such a way that they are dependent on both T_{in} and ΔT_{max}.

Different from the HODF case, the autoignition time is nearly the same over the whole studied region, with a slight dependence only on the inlet temperature, as indicated by the vertical iso-lines. Similar to the HODF case, the overlapping of the steady (feedback and no-combustion zone) and unsteady regimes is not perfect in the case of HFDF. The two domains differ from the blue dashed area, which partly covers the transitional black-dashed area also shown in Figure 5.23.

The results reported above show that he domains of MILD combustion of the unsteady reactive mixing layer are smaller in comparison to the corresponding domains under steady HODF/HFDF conditions. The maximum ignition delays reported in Figures 5.22 and 5.23 were $20\,ms$ and $0.5\,ms$, respectively. None of the regions on the left sides of these autoignition delays yielded any transient reactive mixing layers. Therefore, steady MILD combustion processes can be stabilized in these regions only if additional heat is provided through recirculation or through a piloted source [35].

The extensions of the regions that cannot be reached by any autoigniting combustion process consist of the black and blue dashed areas in Figures 5.22 and 5.23.

Notably, the boundaries of the areas, including the high-temperature combustion regions, where a combustion process could be stabilized only under steady conditions, are much wider for the HFDF than for the HODF, and they closely follow the trends of the characteristic times of the processes.

The most reactive mixture fraction, Z_{MR}, is always positioned on the high-temperature side with respect to the stoichiometric mixture fraction for both HODF and HFDF.

The process evolution rate of unsteady MILD combustion is not universal. In fact, at least in the two of the analyzed cases, the process evolution rates are

just the opposite. In HODF conditions, the overall rates slow down passing into the MILD combustion domain as shown by the characteristic times reported in Figure 5.21. The characteristic autoignition, maximization and stabilization times are all longer than those in high-temperature combustion processes. This situation is the opposite for HFDF conditions. The unsteady diffusive autoignition is always shorter than those in the corresponding HODF conditions. Furthermore, the subsequent part of the process accelerates the passage into the MILD combustion domain.

The autoignition delay times in MILD combustion regimes also vary according to external parameters (preheating temperature and dilution level), in agreement with the trends presented by previous authors [36,37].

In conclusion, it is possible to emphasize that the results reported here support the inclusion of an additional property for the characterization of MILD combustion, i.e., a property that accounts for the fact that this process can be auto-sustained with autoignition.

Nevertheless, the whole process must be analyzed not only in terms of the autoignition time but also in terms of the evolution of the oxidation. The presumed slowness of the autoignition process is not universal because it depends on which part of the reactants is under the high-temperature conditions.

Chapter 6

Discussions and Conclusions

The first part of discussion is devoted to give relevance to the following three points:

a) frame-working different parts of the thesis, in particular those presented in sections of methods and results;
b) the general common approach of dimension reduction for the different sub-process;
c) the relevance of the DNS-evaluated transitional flow in this kind of framework.

a) Concerning the first point (a) it is noteworthy to mention the general approach in order to give prediction of the reacting mixing flows. This is has been named MultiSECtioning and it can be described in this way.

Such strategy could be named "MultiSECtioning" Process Evaluation Strategy and it refers also to the intrinsic multi-characteristics of combustion processes. The acronym evokes that the procedure consists in sectioning the whole process in parts, by means of both geometrical sectioning of the control volumes and/or selection of a subset of physical effects, which can be modeled and validated when added ones at the time to the process. The sequential structure of this approach is shown in Figure 6.1. This strategy has an important feature, i.e. it is realistic and quantifiable in its realism. This is not a trivial requirement since the validation of high level model is rarely done without suitable adjustment of parameters or even adjustment of some of its components. In this strategy, the validation has been performed in a knowledgeable way by selecting representative samples of cases to be used for a

thorough evaluation of carefully selected sub-models sets on the basis of their features and of their potential interaction with the model core.

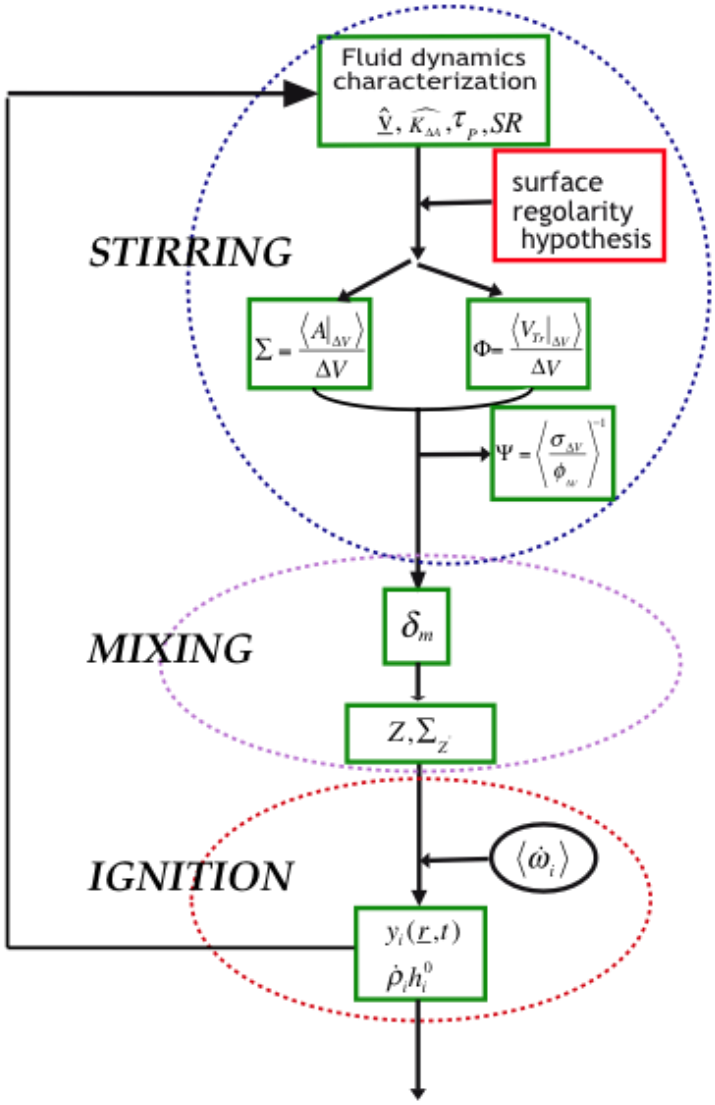

Figure 6.1. Main sequential blocks of the "MultiSECtioning" strategy.

The role of interlinking among different sub-processes has to be carefully evaluated since it can prevent the isolation of functional dependences on controlling parameters that has to be studied by introducing unpredictable

feedback mechanisms acting in different ways in physical and numerical models respectively.

The procedure consists in sectioning the whole process in parts, by means of geometrical sectioning of the control volumes or selection of a subset of one or more physical effects, which can be separately modeled and are, hence, separately validated.

In line of principle only for these sequential processes it is possible to check the accuracy of the numerical predictions through the comparison with the experimental data "side by side" for the two stages in which the whole combustion process has been sectioned. In other words, the validation, made separately for the two parts, is sufficient to ensure a reasonable prediction also for the whole process. Furthermore also the sensitivity analysis in respect to the initial and intermediate parameters is easy to be performed and the experimental and numerical results can support each other in the complete description of the system.

Of course, this is true only for sequential processes and in the case each single sub-process can be successfully described.

On the ground of these considerations, a MultiSECtioning methodology has been conceived because it allows for the analysis of the influence of single sub-processes.

The passage from one part to the other is sketched in Figure 6.1 as block diagram and it allows a sequential combination of the separated effects" and the appropriate characterization of the field obtained by the introduction of new "separated effect".

The first part of the procedure is a fluid-dynamic characterization of the patterns of interest when not reacting flows are introduced in fixed control volume, for fixed boundary-initial conditions, for fixed external parameters.

The fluid dynamic database, generated in this first step, has to be suitable for the characterization of the effects generated by considering the injection of

non-diffusing tracers in the control volume. This is reported in Figure 6.1 in the block quoted as “stirring”.

A large part of this thesis work has aimed to the characterization of this sub-process, which in turn yield interface between the two reactants. In particular, the identification of these surfaces can be seen as the “sinew” of this approach.

This expression summarizes a twofold concept:

- the characterization of advected-surfaces is the “skeleton” of this strategy and it is connected to the other step;
- the interface identification is the mainstay of this kind of approach. The strength of MultiSECtioning is derived from this stage. In this sense, the subsequent steps are a consequence of the first one.

In fact, without a good prediction of the stirring phenomena, the whole combustion process cannot be analyzed in a correct way.

In synthesis it is straight in this context to understand that the evaluation of the stirring characteristics correspond to the first part of the sequential steps briefly listed. In some respect the recognition of such MultiSECtioning strategies is the motivation to investigate the details of the stirring, but it is part of the conclusion which can be drawn from the results. In fact the focusing of well-defined quantities is itself an achievement. Similarly the implicit measurability feasibility, at least in a DNS context is also an indirect achievement. It is relevant also the measurability and the “moldability” of statistical properties which is dealt at point c). These achievements apply to evaluations of both stirring quantities and to autoignition characteristics. In fact they are critical parts of the whole MultiSECtioning strategies and the recognition, that evaluations are possible for both processes, give new perspective to the strategy. Beyond comments and conclusions, totally inside

each part of the thesis, it is mandatory to stress that the two chosen sub-process representative of two parts of the "strategies" have been resulted appropriated. In fact the flow does not undergo large scale recirculation flow which can give stabilization of the combustion process which in turn involves not only the two reactants but also the combustion product. At the same time the boundary conditions of the two reactants and the auto-igniting time evaluated for the different feeding conditions are all compatible with the stirring process. As matter of fact the residence time, autoignition times and oxidation times are comparable in part of the range which make the two boundary/initial conditions choices reciprocally supporting

b) The second point which is interesting to comment and which is shared to both sub-process (stirring and autoignition) is that the two processes has been described with minimum level dimensionality which allow both to preserve and to evaluate the main characterizing properties of the process. The transitional two dimensional flows presented varieties of vortex structures which allow a wide characteristics of statistics. The auto-igniting layerlets evolved along 1-D space coordinate with wide characteristics too. This is relevant because, apart the sectioning of the process envisaged by the MultiSECtioning strategy, this allows to reduce the computation cost if they are very representative of class of flows and of igniting process which evolve on 3-D space. This is not fully proven in this thesis also referring to specific configuration but the a low dimension manifold is exemplified and this enriches the class of both stirring and autoignition conditions. In other words the two processes constitute a conceptual model for describing more complex isothermal and reacting flows.

It is worthwhile to emphasize that the space dimensionality reduction pertain not only the choice of the 2-D conditions for the simulation of the transitional flow but also the choice of representing the whole mixing pattern

starting from the interface. The interface is a surface for a 3-D flow and it is a line for a 2-D flow. In this respect the interface is a way to infer a dimensionality reduction more than a simple feature extraction, therefore a very detailed description of the interface also with higher resolution than that used in the Eulerian characterization of the flow can be achieved with the same computational/data collection limitation. The construction of the interface for a given Eulerian assigned pattern has to be considered a sort of manifold learning process rather than a simple sequential decoupled numerical evaluation.

c) Concerning the third point (c) about the relevance of the DNS in evaluation of the mixing it has only to be add that this choice has been suitable because it also mimics the relevant parts of the LES information in characterization of interface in the sense that both classes of simulations belong to the more wider class of "Eddy Resolving Simulations". In other words the constraints which apply to DNS-interface are the same than those could be obtained by LES. This is confirmed in the framework of DNS, but it can be extended in a methodological sense also to LES since the following basic properties of the interface have to be always be valid and are well described in the super grid part of the LES as well as in the DNS

- interface is continuous
- interfaces are not intersecting
- interface is oriented

Therefore the detection both of single folding events and of their statistical descriptors (in particular the stretch ratio) can suggest the same simplified mappings for taking into account the number of folding times in both kinds of simulations.

These constraints are also relevant in determining which kind of properties are more convenient to be evaluated and which kind of sub-models are more suitable for determining these properties. In other words, even though the analysis is here based on DNS simulation with lower Re it can be transposed "mutatis mutandis" also on data base generated by LES. In particular identification of mixing regimes can be based on the same criteria obtained with this hybridization procedure based on the use of Eulerian/Lagrangian quantities like residence time and stretch ratios. Other field of common (for Eddy Resolution Models) exploitation of the procedure are the criteria for space zoning and equation sectioning .

The second part of discussion is devoted to give relevance to the stirring process analysis of a transitional jet in a 2-D co-flow configuration.

2-D flow systems are suitable to study complex mixing fields in isothermal and reactive conditions. In fact random characteristics either of spatial distribution of scalar quantities, as temperature and concentration, or of fluid-dynamic structures, affecting these quantities in turbulent diffusion flames may be obtained in 2-D time-dependent flows. This is due to the basic principle that chaotic flows can be created also in laminar deterministic periodic conditions. The only additional requirement is that stagnation points have to be distributed in such a way, respect to a reference frame moving with the average velocity, that the stretch ratio of material lines undergo exponential evolution. The high level of stretching is the main feature of dissipative highly diffusive turbulent flow, i.e. the most important factor for increasing mixing rate, consequently combustion rates, and extinguish-related effects.

The other requirements, which 2-D time-dependent flows have to fulfill in order to be representative of 3-D turbulent flow, is the high level of convolution of interfaces, and their distribution on different length scales. The only concern is related to the capability of 2-D flows of being exhaustive in containing all possible fluid-dynamic structures, which are present in 3-D turbulent flows.

In such a view, analysis of the intermaterial surface temporal evolution reported in in Chapter 5 describing the transitional jet behavior in a 2-D co-flow configuration, revealed a key feature of the fluid-dynamic structures related to such a flow.

For a such a case (2-D), in fact, the nature of the vortex structure generated can only formed other vortex structure. In order to give an assessment of the great variety of structures which can be established in 2-D flows, in Chapter 5 all the identified structures (2-D) have been categorized as follow:

- no vortex structure;
- structure associated with the onset of a vortex structure formation;
- simple vortex structure with small number of convolution;
- simple vortex structure highly convoluted;
- simple vortex structure highly convoluted and with braids;
- 2-D counter-rotating vortex couples structure;
- macro-vortex;
- 2-D counter-rotating vortex couples structure within a macro-vortex structure.

It is of great interest to underline that the comparison with structures detected experimentally is quite satisfactory and that, in turn, this shows the 2-D of the flows.

Among the structures highlighted by intermaterial surface description, there are some of them, in which the interfaces (discontinuity between black and white regions in the experiment, particles trajectories in the simulation) are quite convoluted. They undergo a relatively intense stretch rate of the order of $100\,s^{-1}$, as it has been reported in Chapter 5. In the context of a

diffusion flame, this stretch rate is not high enough to cause flame extinction, but it is sufficient for high level of convolution.

The case analyzed, here described, suggests that ensemble of structures, i.e. a simple multi-scale system, can be used in order to explore all possible evolution of the system itself.

However, although analysis revealed a large number of structures, which are also features of a 3-D flow, the question about if a 2-D flows is capable in being exhaustive in containing all possible fluid-dynamic structures, which are present in 3-D turbulent flows remains still open and further simulations (i.e. different jet Re) need to be addressed in order to extend our "topological structures" database.

Analysis of residence time and SR reported in Chapter 5 showed that such a quantities grow almost linearly with nozzle distance and time, respectively. Furthermore trend analysis highlighted that they are not subjected to a strong fluctuations. This is due to the fact that particles residence time and SR are cumulative time-averaged quantities, therefore, they are already itself not associated to strong fluctuations. It has been pointed out in Chapter 5 that SR fluctuations can be attributed to a sequential events of extension/compression of intermaterial surface. It is important to remind that configuration analyzed (jet in a co-flow configuration) is realized in order to induce mixing, thus, SR is always higher then 1. In order to support such a thesis, Figure 6.2 reports the evolution of an intermaterial surface element. It is worthwhile to note that such a element is not subjected to a stretch as long as is not located within a vortex. Furthermore, it shows its maximum extension in the intra-vortex region (in between two different vortex structure) and is undergoes a contraction either when it leaves a vortex or just before entering in it.

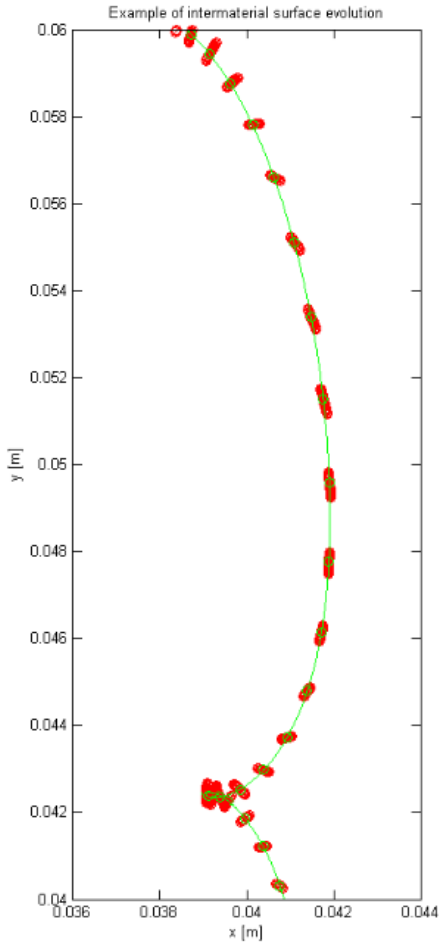

Figure 6.2. Evolution of an intermaterial surface element.

Another feature of the system reported in Chapter 5 is that the stretch rate, K_{SR}, remains almost constant with time. Such a trend suggested that the deformation of an intermaterial surface (for the system under investigation) is not a function of the time (deformation is not dependent of time). Analysis of the mean stretching (or squeezing) factor in the region characterized by an higher vorticity (cells more statistically relevant) supports this thesis. In fact, in such a region the value of stretching factor is close to 1; in other words such a region is associated to an approximately constant stretch rate, with a balance between extensions and contraction of the intermaterial surface.

Finally, analysis of layer thickness highlighted that is of the order of $10^{-2}\,m$. Such analysis can be helpful also for obtaining information about a reactive system. They can be derived following [3]. Here, it has been reported that $\delta_r \cong 5\sigma\delta_m$, i.e. the reactive layer is equal to the thickness of the diffusive layer multiplied by five times the thickness of the flame in the mixture fraction domain (σ). The σ value for fuels as methane or hydrogen has been evaluated to be less than 0.02; thus δ_r is less than $\delta_m/10$. A numerical example can give some idea of the possible extension of δ_r. Let us consider the case in which the diffusive layer evolves over a time of one second and that the diffusion coefficient is $\mathcal{D} = 10^{-5}\,m^2 s^{-1}$, δ_m will extend for $10^{-2}\,m$, whilst the reactive layer (for a paraffin) would be in the order of $10^{-3}\,m$.

The case reported and described in this thesis suggests that ensemble of structures, i.e. a simple multi-scale system, can be used in order to explore all possible evolution of the system itself. together with the following one, shows how this tool can be exploited to identify mixing isothermal regimes and to give statistical averages of the most relevant parameter affecting a reactive system (i.e. diffusion flames) and a isothermal transitional flow.

The third part of discussion is devoted to give relevance to analysis of a 1-D reactive system evolving under MILD Combustion condition.

The results reported in Chapter 5 show that the domains of MILD combustion of the unsteady reactive mixing layer are smaller in comparison to the corresponding domains under steady HODF/HFDF conditions. The maximum ignition delays reported in Chapter 5 highlighted that none of the regions on the left sides of these autoignition delays yielded any transient reactive mixing layers. Therefore, steady MILD combustion processes can be stabilized in these regions only if additional heat is provided through recirculation or through a piloted source [35].

The extensions of the regions that cannot be reached by any auto-igniting combustion process consist of the black and blue dashed areas. Notably, the boundaries of the areas, including the high-temperature combustion regions, where a combustion process could be stabilized only under steady conditions, are much wider for the HFDF than for the HODF, and they closely follow the trends of the characteristic times of the processes.

The most reactive mixture fraction is always positioned on the high-temperature side with respect to the stoichiometric mixture fraction for both HODF and HFDF.

The process evolution rate of unsteady MILD combustion is not universal. In fact, at least in the two of the analyzed cases, the process evolution rates are just the opposite. In HODF conditions, the overall rates slow down passing into the MILD combustion domain as shown by the characteristic times reported in Figure 5.21. The characteristic autoignition, maximization and stabilization times are all longer than those in high-temperature combustion processes. This situation is the opposite for HFDF conditions. The unsteady diffusive autoignition is always shorter than those in the corresponding HODF conditions. Furthermore, the subsequent part of the process accelerates the passage into the MILD combustion domain.

The autoignition delay times in MILD combustion regimes also vary according to external parameters (preheating temperature and dilution level), in agreement with the trends presented by previous authors [36,37].

In conclusion, it is possible to emphasize that the results reported here support the inclusion of an additional property for the characterization of MILD combustion, i.e., a property that accounts for the fact that this process can be auto-sustained with autoignition.

Nevertheless, the whole process must be analyzed not only in terms of the autoignition time but also in terms of the evolution of the oxidation. The presumed slowness of the autoignition process is not universal because it

depends on which part of the reactants is under the high-temperature conditions.

The fourth part of this section is eventually presented in order to synthesize the first three parts of this discussion as well as to give preliminary ensemble of conclusions related to 2-D transitional flows studied in the thesis. The generalization to all classes of 2-D transitional flows or to the whole class of 2-D flows are explicitly mentioned when this is possible.

1. The methodological part for the analysis of the stirring characteristics outlined in this thesis is of some practical interest since great part of the quantities involved in this analysis can be evaluated inside a frame of eddy resolving models along the exemplificative patterns outlined in this 2-D analysis apart some case mentioned in the following.

2. Interface topology in a 2-D transitional flow is mainly characterized by interface peninsulas which in great part of the events are arranged in single or multiple vortices. This is the case of the conditions analyzed in this thesis, but the generalization is possible on the ground of the surface constraint (continuity and not intersection) which has been taken into account. On the opposite there is at the moment no possible generalization of the interface distances (or of equivalent quantity like the surface density).

3. The average residence times of points sampled on the interfaces are uniformly distributed along the radial direction of the jet and their probability density functions can be approximated by continuous distribution with only secondary modal peaks which emerge on a continuous pedestal. This characteristic seems to be sharable by all the eddy structures for whatever 2-D condition because the trajectory of

the points which are involved in the eddy structures develop along linear paths which are more or less extended according to which parts of the vortex are reached.

4. The average stretch rates of points sampled on interfaces have outstanding low values even though single event can reach relatively high values. This can be considered a general characteristic for 2-D flows because the compressive and extensive gradient for incompressible flows have to be equal in whatever 2-D flows. Therefore the alignment of a positive stretching flows with the interface could occur because of the particular choice of the boundary conditions. This characteristic is difficult to be generalized to 3-D flows.

5. This last characteristic is relevant in the analysis of the stabilization of diffusion flames. In fact it is well known that high stretch rates are capable of quenching the combustion process. This is not the case when one of the reactant has very high temperature. This critical aspect has been analyzed in a special deepening of diffusive reactive structure with high temperature reactant. The main result is that also high value of stretch rates do no quench the reactive structures therefore the stirring analysis presented in this thesis has a high interest in this type of flows because the reaction structure exist and the integral values of the quantities presented here are the process controller. In particular the stretch ratio which is the temporal integral of the stretch rates is the controlling parameter of the mixing rate and its correspondent reactive regimes for a large spectrum of boundaries conditions.

References

[1] Williams FA. Combustion theory. Benjamin/Cummings. Menlo Park, CA 1985.

[2] Kuo K. Principles of combustion. Wiley. New York 1986.

[3] Cavaliere A, Ragucci R. Gaseous diffusion flames: simple structures and their interaction. *Progress in Energy and Combustion Science*, 27(5):547-585, 2001.

[4] Ottino JM. Description of mixing with diffusion and reaction in terms of the concept of material surfaces. *Journal of Fluid Mechanics*, 114:83-103, 1982.

[5] Crowe CT, Chung JN, Troutt TR. Particle mixing in free shear flows. *Progress in Energy and Combustion Science*, 14(3):171-194, 1988.

[6] Rosner DE. Transport processes in chemically reacting flow systems (p. 123). Butterworths. Boston, MA 1986.

[7] Aref H. Stirring by chaotic advection. *Journal of Fluid Mechanics*, 143:1-21, 1984.

[8] Chaiken J, Chu CK, Tabor M, Tan QM. Lagrangian turbulence and spatial complexity in a Stokes flow. *Physics of Fluids*, 30:687-694, 1987.

[9] Cavaliere A, El-Naggar M. Experimental analysis of intermaterial surfaces in the study of gaseous mixing characteristics. *International Journal of Heat and Mass Transfer*, 38(2):317-319, 1995.

[10] Pope SB. The evolution of surfaces in turbulence. *International Journal of Engineering Science*, 26(5):445-469, 1988.

[11] Gibson CH. Fine Structure of Scalar Fields Mixed by Turbulence: I. Zero-Gradient Points and Minimal Gradient Surfaces. *Physics of Fluids*, 11:2305-2315, 1968.

[12] Sorrentino G, Ragucci R, Cavaliere A. Investigation of the stirring process in a turbulent jet by means of Particle Image Velocimetry. *16th International Symposium on Applications of Laser Techniques to Fluid Mechanics*, Lisbon, Portugal, 09-12 July, 2012.

[13] Marble, Frank E., and James E. Broadwell. The coherent flame model for turbulent chemical reactions. No. SQUID-TRW-9-PU. PURDUE UNIV LAFAYETTE IN PROJECT SQUIDHEADQUARTERS, 1977.

[14] Van Kalmthout, E., D. Veynante, and S. Candel. Direct numerical simulation analysis of Blame surface density equation in non-premixed turbulent combustion. Symposium (International) on Combustion. Vol. 26. No. 1. Elsevier, 1996.

[15] Ottino, JM, 1981, EfBiciency of mixing from data on fast reactions in multi-jet reactors and stirred tanks. AICh.EJ 27, 184 192.

[16] Ottino, J. M. Mixing, chaotic advection, and turbulence. Annual Review of Fluid Mechanics 22.1 (1990): 207-254.

[17] Chella, R., and J. M. Ottino. "Conversion and selectivity modifications due to mixing in unpremixed reactors." Chemical engineering science 39.3 (1984): 551-567.

[18] Lefebvre, A. H. 1989 Atomization and Sprays.

[19] Cavaliere A, El-Naggar M, Ragucci R. Experimental identification of mixing regimes in the analysis of turbulent diffusion flames. *Combustion and Flame*, 99(3-4):679-686, 1994.

[20] Tropea C., Annu. Rev. Fluid Mech., 2011.

[21] Melling, A. Tracer particles and seeding for particle image velocimetry. Measurement Science and Technology 8.12 (1999): 1406.

[22] Sorrentino G. Characterization of advected-surfaces. The sinews of a "MultiSECtioning" approach for non-premixed combustion. Ph. D. Thesis, 2013.

[23] Haller G. An objective definition of a vortex. *Journal of Fluid Mechanics*, 525:1-26, 2005.

[24] Green MA, Rowley CW, Haller G. Detection of Lagrangian coherent structures in three-dimensional turbulence. *Journal of Fluid Mechanics*, 572:111-120, 2007.

[25] Pope SB. Turbulent Flows. Cambridge University Press. Cambridge, UK 2000.

[26] Crowe CT, Schwarzkopf JD, Sommerfeld M, Tsuji Y. Multiphase Flows with Droplets and Particles. CRC Press. Boca Raton, FL 2011.

[27] Andersson B, Andersson R, Hakansson L, Mortensson M, Sudiyo R, van Wachem B. Computational Fluid Dynamics for Engineers. Cambridge University Press. Cambridge, NY 2011.

[28] Batchelor GK. An Introduction to Fluid Dynamics. Cambridge University Press. Cambridge, England 1967.

[29] Shepard D. A two-dimensional interpolation function for irregularly-spaced data. *Proceedings of the 1968 ACM National Conference*, 517–524, 1968.

[30] Rice RG, Do DD. Applied Mathematics and Modeling for Chemical Engineers. John Wiley & Sons, Inc. USA 1995.

[31] Tabakoff W, Wakeman T. Measured particle rebound characteristics useful for erosion prediction. *American Society of Mechanical Engineers, International Gas Turbine Conference and Exhibit, 27th,* London, England 1982.

[32] Boffetta G. & Ecke R.E. (2012). Two-dimensional turbulence. Annual Review of Fluid Mechanics, 44, 427-451.

[33] Parente, A., C. Galletti, and L. Tognotti. Effect of the combustion model and kinetic mechanism on the MILD combustion in an industrial burner fed with hydrogen enriched fuels. International journal of hydrogen energy 33.24 (2008): 7553-7564.

[34] Mastorakos, E. (2009). Ignition of turbulent non-premixed Blames. Progress in Energy and Combustion Science, 35(1), 57-97.

[35] Abtahizadeh, Seyed Ebrahim, Jeroen van Oijen, and Philip de Goey. Numerical study of a jet-in-hot-coBlow burner with hydrogen-addition using the Flamelet Generated Manifolds technique. Bulletin of the American Physical Society 57 (2012).

[36] Liu, Shiling, et al. Effects of strain rate on high-pressure nonpremixed n-heptane autoignition in counterBlow. Combustion and Blame 137.3 (2004): 320-339.

[37] Mastorakos, E., T. A. Baritaud, and T. J. Poinsot. Numerical simulations of autoignition in turbulent mixing Blows. Combustion and Flame 109.1 (1997): 198-223.